



Periodic Fast Radio Bursts from Luminous X-ray Binaries

Navin Sridhar^{1,2} , Brian D. Metzger^{2,3} , Paz Beniamini^{4,5} , Ben Margalit^{6,10} , Mathieu Renzo^{2,3} , Lorenzo Sironi^{1,2} , and Konstantinos Kovlakas^{7,8,9}

¹ Department of Astronomy, Columbia University, New York, NY 10027, USA; navin.sridhar@columbia.edu

² Columbia Astrophysics Laboratory, Columbia University, New York, NY 10027, USA

³ Center for Computational Astrophysics, Flatiron Institute, 162 W. 5th Avenue, New York, NY 10011, USA

⁴ Division of Physics, Mathematics and Astronomy, California Institute of Technology, Pasadena, CA 91125, USA

⁵ Astrophysics Research Center of the Open University (ARCO), The Open University of Israel, P.O. Box 808, Raanana 43537, Israel

⁶ Astronomy Department and Theoretical Astrophysics Center, University of California, Berkeley, Berkeley, CA 94720, USA

⁷ Geneva Observatory, University of Geneva, Chemin des Maillettes 51, 1290 Versoix, Switzerland

⁸ Physics Department, University of Crete, GR 71003, Heraklion, Greece

⁹ Institute of Astrophysics, Foundation for Research and Technology-Hellas, GR 71110, Heraklion, Greece

Received 2021 March 1; revised 2021 May 12; accepted 2021 May 12; published 2021 August 9

Abstract

The discovery of periodicity in the arrival times of the fast radio bursts (FRBs) poses a challenge to the oft-studied magnetar scenarios. However, models that postulate that FRBs result from magnetized shocks or magnetic reconnection in a relativistic outflow are not specific to magnetar engines; instead, they require only the impulsive injection of relativistic energy into a dense magnetized medium. Motivated thus, we outline a new scenario in which FRBs are powered by short-lived relativistic outflows (“flares”) from accreting black holes or neutron stars, which propagate into the cavity of the pre-existing (“quiescent”) jet. In order to reproduce FRB luminosities and rates, we are driven to consider binaries of stellar-mass compact objects undergoing super-Eddington mass transfer, similar to ultraluminous X-ray (ULX) sources. Indeed, the host galaxies of FRBs, and their spatial offsets within their hosts, show broad similarities with ULXs. Periodicity on timescales of days to years could be attributed to precession (e.g., Lens-Thirring) of the polar accretion funnel, along which the FRB emission is geometrically and relativistically beamed, which sweeps across the observer line of sight. Accounting for the most luminous FRBs via accretion power may require a population of binaries undergoing brief-lived phases of unstable (dynamical-timescale) mass transfer. This will lead to secular evolution in the properties of some repeating FRBs on timescales of months to years, followed by a transient optical/IR counterpart akin to a luminous red nova, or a more luminous accretion-powered optical/X-ray transient. We encourage targeted FRB searches of known ULX sources.

Unified Astronomy Thesaurus concepts: Radio transient sources (2008); Ultraluminous X-ray sources (2164); X-ray binary stars (1811); Shocks (2086); Plasma astrophysics (1261); High energy astrophysics (739); Burst astrophysics (187); X-ray transient sources (1852)

1. Introduction

Fast radio bursts (FRBs) are short, luminous pulses of coherent radio emission of extragalactic origin (Lorimer et al. 2007; Keane et al. 2012; Thornton et al. 2013). Among the many proposed FRB models (Platts et al. 2019), the best-studied are those that postulate flaring magnetars as their central engines (e.g., Popov & Postnov 2013; Kulkarni et al. 2014; Lyubarsky 2014; Katz 2016; Metzger et al. 2017; Beloborodov 2017; Kumar et al. 2017; Metzger et al. 2019; Wadiasingh & Timokhin 2019). Magnetar models can account for many observed properties of FRBs, including their short (\lesssim millisecond) timescales, large energetics, potentially high polarization (e.g., Michilli et al. 2018; Luo et al. 2020), ability to recur (e.g., Spitler et al. 2016; CHIME/FRB Collaboration et al. 2019), and frequent association with star-forming host galaxies (Tendulkar et al. 2017; Bhandari et al. 2020; Heintz et al. 2020; Li & Zhang 2020; Mannings et al. 2020; Safarzadeh et al. 2020; Bochenek et al. 2021). Magnetar models have also received support from the discovery of an FRB-like radio burst from the Galactic magnetar SGR1935 + 2154 (The CHIME/FRB Collaboration et al. 2020; Bochenek et al. 2020) in coincidence with a luminous, hard X-ray flare (e.g., Mereghetti et al. 2020; Li et al. 2021).

Despite these many successes, magnetar models are not without challenges:

1. No confirmed magnetars (of the kind observed in our Galaxy and Local Group) are sufficiently active to explain the recurring FRB sources, such as FRB 121102 (e.g., Spitler et al. 2016) or the population of repeaters discovered by CHIME/FRB (e.g., CHIME/FRB Collaboration et al. 2019). This is despite the fact that similarly active repeaters contribute a significant fraction of the total FRB rate, including the (currently) non-repeating population (Margalit et al. 2020; Lu et al. 2020). Such behavior could be explained by invoking a younger and/or more active magnetar population, possibly with even stronger internal magnetic fields than those of known Galactic magnetars (e.g., Beloborodov 2017). This required source population could even be the product of one or more rare formation channels (e.g., exotic supernovae, hereafter SNe, binary neutron star (NS) or NS-white dwarf mergers, or accretion-induced collapse of a white dwarf; Metzger et al. 2017; Margalit et al. 2019; Zhong & Dai 2020; Margalit et al. 2020), but these possibilities are currently speculative.
2. The two best-studied repeating sources, FRB 180916 and FRB 121102, show periodicities in their burst arrival times of ~ 16 and ~ 160 days, respectively (Chime/Frb Collaboration

¹⁰ NASA Einstein Fellow.

et al. 2020; Rajwade et al. 2020). Again, several plausible ideas were proposed to generate periodic behavior within magnetar and highly magnetized pulsar scenarios (precession, binarity, extremely slow rotation, orbital motion; Lyutikov et al. 2020; Beniamini et al. 2020; Levin et al. 2020; Zanazzi & Lai 2020; Ioka & Zhang 2020; Li & Zanazzi 2021). However, these would all be novel, as no confirmed magnetars exhibit these properties.

3. Magnetar activity is ultimately limited by the energy contained in their strong magnetic fields. This budget becomes strained once realistic radiative efficiencies for the FRB emission (e.g., Plotnikov & Sironi 2019; Chen et al. 2020) are combined with the long observed active lives of some repeating sources (approaching a decade for FRB 121102; Cruces et al. 2021).
4. One of the nearest repeating source, FRB 180916, is spatially offset in its host galaxy from the closet region of active star formation (Tendulkar et al. 2021). While consistent with the demographics of larger FRB samples (e.g., Mannings et al. 2020; Heintz et al. 2020), this location is in tension with scenarios that invoke young (age $\lesssim 10$ kyr) magnetars formed in core collapse SNe (Tendulkar et al. 2021).

Even within magnetar scenarios, there exist distinct models that invoke different physical mechanisms and emission regions for generating the FRB emission (e.g., Zhang 2020a for a review). These can be broadly divided into “magnetospheric” scenarios (in which the emission originates close to the NS surface; Kumar et al. 2017; Kumar & Bošnjak 2020; Wadiasingh & Timokhin 2019; Wadiasingh et al. 2020) and “shock” scenarios (in which the emission originates in a relativistic outflow at much greater distances; Lyubarsky 2014; Beloborodov 2017; Plotnikov & Sironi 2019; Metzger et al. 2019).

While magnetospheric scenarios may be exclusive to NS engines, shock scenarios apply to a wider range of central-engine models. As emphasized by Metzger et al. (2019), a basic requirement of the latter is simply the impulsive injection of ultra-relativistic energy into a strongly magnetized medium of the appropriate density (one example being the relativistic wind from the terminal stage of a binary NS merger; Sridhar et al. 2021). Models in which FRBs are powered by magnetic reconnection in a relativistic magnetized outflow (e.g., Lyubarsky 2020) may be similarly agnostic to a magnetar as the specific engine triggering the energy release.

All of this motivates us to consider other central engines, whose more continuous activity, longer timescales (e.g., binary orbit related), and greater energy reservoirs, concur more with the natural features of FRBs. An obvious candidate explored in this paper are *accreting* stellar-mass compact objects, such as NSs or black holes (BHs), which are known to generate energetic and dynamical activity powered by strong magnetic fields carried in or generated by the accretion flow (e.g., Fender et al. 2004). Accretion-powered FRB engines of this broad class were previously discussed by Waxman (2017) and Katz (2017, 2020). As we shall demonstrate, the dual requirements to account for observed FRB timescales and luminosities drive us to the regime of super-Eddington accretion, for which the closest known observational analogs are the “ultraluminous X-ray” sources (ULXs) that are typically characterized by super-Eddington luminosities (see Kaaret et al. 2017 for a review). As we proceed, we shall therefore draw connections

between the phenomenology of FRB and ULX sources. Figure 1 is a schematic diagram of the envisioned scenario.

This paper is organized as follows. Section 2 places basic constraints on accretion scenarios and outlines a potential FRB mechanism. Section 3 discusses the types of binary systems that give rise to the requisite accretion rates and source formation rates. Section 4 outlines additional predictions of the scenario such as host galaxies and multiwavelength counterparts. We conclude by summarizing the predictions of the model in Section 5.

2. Basic Constraints

This section outlines the characteristics an accreting central engine must satisfy in order to explain the basic observed properties of FRBs. For this, we consider a compact object (fiducially a BH) of mass M , accreting at a rate \dot{M} , which we shall normalize to the Eddington accretion rate as $\dot{m} \equiv \dot{M}/\dot{M}_{\text{Edd}}$, where $\dot{M}_{\text{Edd}} \equiv L_{\text{Edd}}/c^2$, $L_{\text{Edd}} = 4\pi GM_*c/\kappa_{\text{es}}$ is the Eddington luminosity, and we take $\kappa_{\text{es}} = 0.38 \text{ cm}^2 \text{ g}^{-1}$ for the electron scattering opacity (Frank et al. 2002).

2.1. Timescale

The characteristic minimum timescale for significant energy release from a BH engine is set by the light-crossing time of the innermost stable circular orbit (ISCO):

$$t_{\text{min}} \sim \frac{R_{\text{ISCO}}}{c} \approx 0.3 \text{ ms} \left(\frac{m}{10} \right) \left(\frac{R_{\text{ISCO}}}{6R_g} \right), \quad (1)$$

where $R_g \equiv GM_*/c^2$ and $m \equiv M/M_\odot$. A similar expression holds in the case of an NS accretor with R_{ISCO} replaced by the NS radius, $R_{\text{NS}} \simeq 12 \text{ km}$ (equivalent to $6R_g$ for $M_* = 1.4 M_\odot$).

It is not obvious a priori that the timescale over which the engine releases energy would match that of an observed FRB. However, this turns out to be approximately true in emission models that invoke dissipation within a transient relativistic outflow (Section 2.5). Generic arguments show that FRBs must be produced in ultra-relativistic outflows (e.g., Lu & Kumar 2018). Consider a relativistically expanding ejecta shell, emitted as a “flare” from the central engine over a timescale $t_f \gtrsim t_{\text{min}}$ with a corresponding thickness $\Delta \simeq c \cdot t_f$, propagating toward the observer with a bulk Lorentz factor $\Gamma \gg 1$. Any process that taps into the energy of the ejecta shell by crossing it at close to the speed of light in the co-moving frame (e.g., a reverse shock or magnetic reconnection) will complete once the shell reaches a radius $r_{\text{FRB}} \sim \Gamma^2 \Delta$. An FRB emitted coincident with this energy release will arrive at an external observer over a timescale $\lesssim r_{\text{FRB}}/2\Gamma^2 \sim t_f$, i.e., roughly matching the original activity time of the central engine¹¹ (see Beniamini & Kumar 2020 for more details). This follows a similar faithful mapping between engine and prompt emission activity in gamma-ray bursts (e.g., Kumar & Zhang 2015).

2.2. Luminosity

The power of the ultra-relativistic component of a BH outflow is given by the Blandford & Znajek (1977, BZ) jet

¹¹ In FRB emission models powered by a shock propagating into a high magnetization $\sigma \gg 1$ medium, the observed emission duration can be shorter than that of the engine by a factor of $1/\sigma$ (e.g., Babul & Sironi 2020; Beloborodov 2020).

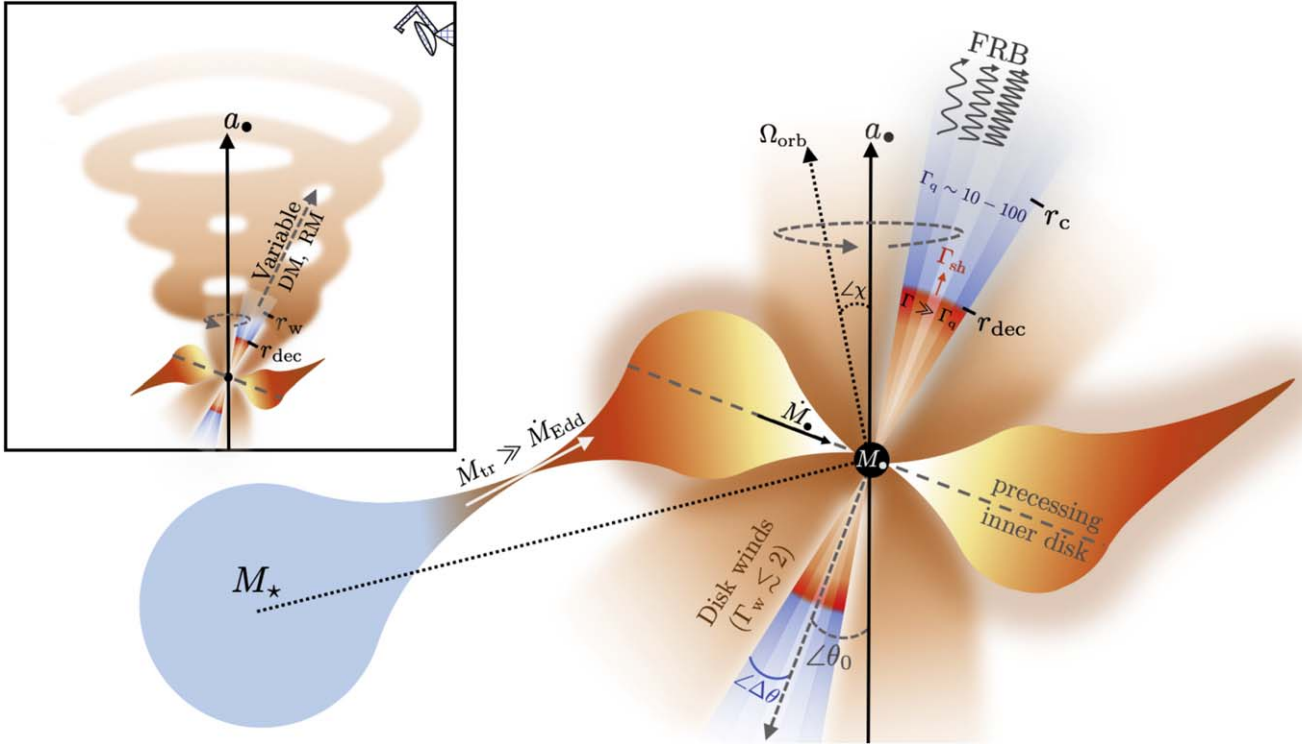


Figure 1. Schematic diagram of the production of periodic FRBs from accretion-powered flares in ULX-like binaries outlined in this paper. A star of mass M_* undergoes thermal- or dynamical-timescale mass transfer onto a compact BH or NS remnant of mass M , at rate \dot{M}_t near or exceeding the Eddington rate. The super-Eddington accretion flow is radiatively inefficient and hence subject to powerful outflows, which can reduce the accretion rate closer to the central compact object, $\dot{M} \ll \dot{M}_t$. The mass-loaded disk winds also shape the narrow polar accretion funnel of half-opening angle $\Delta\theta$ and corresponding beaming fraction f_b . FRB emission is generated by a relativistic flare of energy released close to the innermost stable circular orbit (e.g., due to reconnection of magnetic field lines threading the BH horizon), which propagates outwards along the accretion funnel as an ultra-relativistic shock into the cavity of the previous “quiescent” jet. Coherent radio emission (the FRB) is generated via the synchrotron maser shock mechanism or magnetic reconnection within the relativistic flow (at radii $\gg r_c$, above which induced Compton scattering in the quiescent jet is negligible; Equation (8)). If the spin axis of the BH is misaligned with respect to the angular momentum axis of the accretion disk, the polar cavity—and hence the direction along which the FRB emission is geometrically beamed—is modulated by Lens-Thirring (LT) precession on a timescale of days to years (Equation (27)). Inset: the magnetized disk outflows are swept into a spiral pattern due to the precession of the disk angular momentum about the axis of BH spin (a_*). The instantaneous jet axis intersects this wind (from an earlier precession phase) on larger scales $\gtrsim r_w$ (Equation (33)). Small systematic variations in the burst dispersion measure (DM) and rotation measure (RM) are expected due to this encounter (Equation (35)).

luminosity, which can be written as (Tchekhovskoy et al. 2011)

$$L_{\text{BZ}} = \eta \dot{M} c^2 \approx \eta \dot{m} L_{\text{Edd}}, \quad (2)$$

where the jet efficiency η depends on the magnetic flux threading the BH horizon and the dimensionless BH spin, a_* . The maximum allowed $\eta = \eta_{\text{max}}$ corresponds to a magnetically arrested accretion disk (MAD), and varies from $\eta_{\text{max}} = 0.3$ (for $a_* \approx 0.5$) to $\eta_{\text{max}} = 1.4$ (for $a_* = 0.99$; Tchekhovskoy et al. 2011). A similar jet luminosity can, in principle, be generated by an accreting NS, although the magnetic flux in this case corresponds to that of the NS surface field, and the dependence of the jet power on accretion rate is more complicated (e.g., Parfrey et al. 2016).

Even absent a large-scale magnetic field of fixed polarity threading the disk, a temporary jet with a power $\sim L_{\text{BZ}}$ can be generated by inflating and opening up small-scale field lines connecting the BH, due to the differential rotation of the accretion flow (e.g., Parfrey et al. 2015; Ripperda et al. 2019; Mahlmann et al. 2020). The instantaneous jet efficiency can therefore in principle also approach L_{BZ} with $\eta \sim \eta_{\text{max}} \sim 1$ for brief intervals even in relatively weakly magnetized disks. This differs from the MAD case insofar that the mean power corresponding to the persistent jet (when the flux from a reconnected magnetic loop is not threading the BH) may be

significantly lower. The “transient” nature of such a jet will turn out to be important in generating an observable FRB signal (Section 2.5).

The most luminous FRB sources will turn out to be rare compared to the super-Eddington accreting BH/NS population as a whole (Section 3.2), thus allowing them to represent the most extreme cases of accreting binaries found in nature (Section 3.2). Taking $\eta \sim \eta_{\text{max}} \sim 1$ may be justified for their most luminous bursts. The maximum isotropic-equivalent radio luminosity of an FRB powered by accretion can thus be written

$$L_{\text{FRB}}^{\text{max}} \approx f_{\xi} f_b^{-1} \eta_{\text{max}} \dot{M} c^2 \sim f_{\xi} f_b^{-1} \dot{m} L_{\text{Edd}} \\ \dot{m} \gtrsim 100.014 \left(\frac{f_{\xi}}{10^{-3}} \right) \left(\frac{\dot{m}}{10} \right)^3 L_{\text{Edd}}, \quad (3)$$

where $f_{\xi} \equiv L_{\text{FRB}}/L_{\text{BZ}}$ is the efficiency of converting the energy of the transient jet into coherent radio emission (e.g., $f_{\xi} < 10^{-2}$ in synchrotron maser scenarios; Section 2.5) and f_b is the beaming fraction. The final line in Equation (3) employs an expression for the X-ray beaming fraction motivated by ULX observations (Equation (4)), an appropriate choice if the FRB is geometrically beamed by a plasmoid ejected along the accretion funnel (Section 2.3).

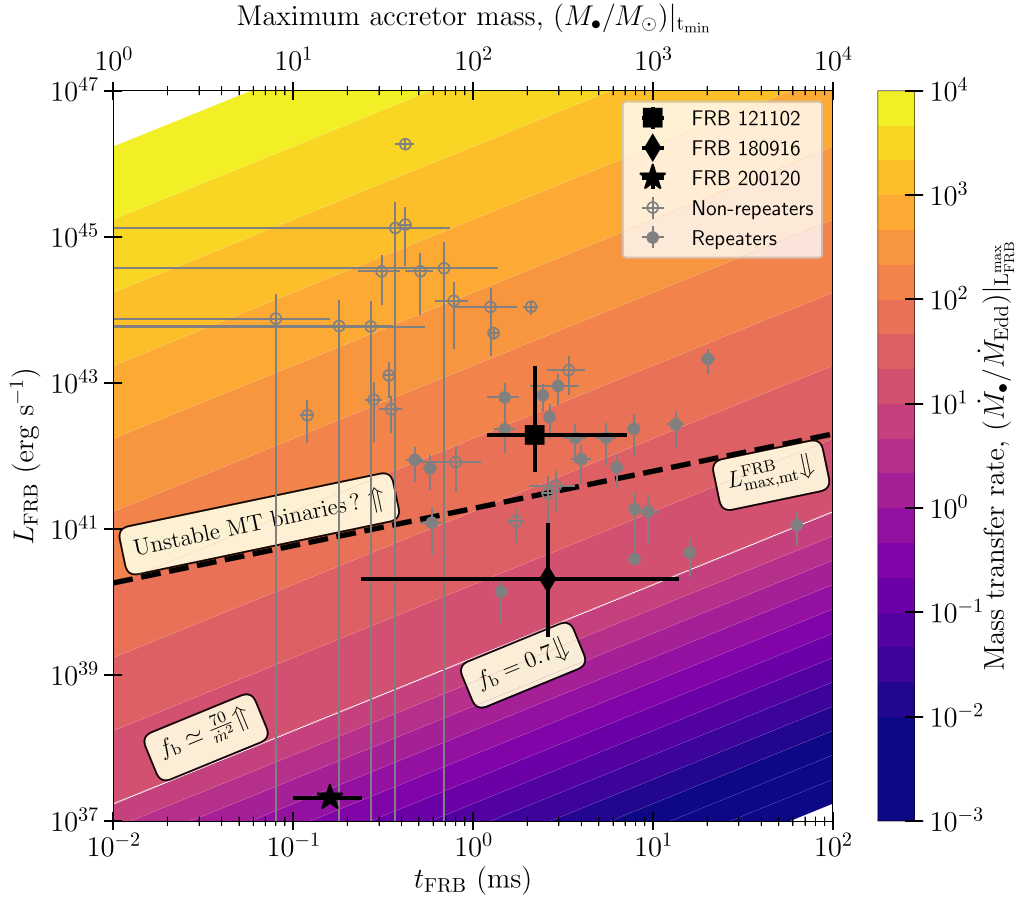


Figure 2. If most of the luminous FRBs are powered by accreting compact objects, the latter must be NSs or stellar-mass BHs accreting near or well above the Eddington rate. Here we show the observed isotropic luminosities and durations of repeating and non-repeating FRBs as filled and non-filled gray circles, including ranges for the repeating sources, FRB 121102 (square), FRB 180916 (diamond; <http://www.frbcat.org>; Petroff et al. 2016), and FRB 200120 (star; Bhardwaj et al. 2021). The top axis shows the NS/BH mass M_\bullet corresponding to the minimum FRB duration t_{\min} (Equation (1)) assuming $R_{\text{isco}} = 2R_g$. Colored contours show the corresponding mass-transfer (MT) Eddington ratio required to achieve an isotropic-equivalent luminosity $L_{\text{FRB}} = L_{\text{FRB}}^{\text{max}}$ (Equation (3)) for an assumed FRB emission efficiency $f_\xi = 10^{-3}$ (Section 2.5) using the value M_\bullet corresponding to the t_{\min} condition, and adopting a beaming fraction (f_b) motivated by ULX observations (Equation (4)). A dashed black line shows the limit corresponding to systems undergoing stable MT accretion (Equation (21)).

Figure 2 shows the observed durations and luminosities of a large sample of FRBs, including the well-studied repeating sources FRB 121102 and FRB 180916, and the nearest extragalactic FRB 200120 (Bhardwaj et al. 2021). The top axis gives the value of M_\bullet corresponding to t_{\min} (Equation (1)) for $R_{\text{isco}} \simeq 2R_g$ (a rough lower limit corresponding to a rapidly spinning BH). Colored contours show the corresponding minimum Eddington ratio \dot{m} required to achieve $L_{\text{FRB}} = L_{\text{FRB}}^{\text{max}}$ (Equation (3)) for an assumed efficiency $f_\xi = 10^{-3}$ using the value M_\bullet corresponding to the t_{\min} condition (Section 2.5). The contours are derived by assuming the beaming fraction motivated by ULX observations (Equation (4) and surrounding discussion).

First, we see that observed durations of most require accretors of mass $M_\bullet \lesssim 10^3 M_\odot$, corresponding to NS or stellar-mass BH engines. In order to explain the most luminous FRBs (particularly the non-repeating sources), we require super-Eddington accretion rates, $\dot{m} \gtrsim 1 - 10^3$. By contrast, the isotropic-equivalent luminosity of FRB 200120—purportedly located in the nearby galaxy M81—is smaller than any other extragalactic FRB by at least three orders of magnitude. Note that this luminosity is consistent with arising from an X-ray binary accreting below the Eddington rate.

2.3. Beaming

Figure 2 demonstrates that the most luminous FRB sources require accretion rates $\dot{m} \gg 1$. Such super-Eddington levels of accretion (Shakura & Sunyaev 1973) correspond to the regime of photon-trapped radiatively inefficient accretion flows (RIAFs; e.g., Katz 1977; Abramowicz et al. 1988; Narayan & Yi 1995; Blandford & Begelman 1999). These systems are characterized by optically and geometrically thick accretion disks with powerful mass-loaded winds (e.g., Begelman et al. 2006; Poutanen et al. 2007) and a narrow open funnel along the polar axis defined by the disk angular momentum. Super-Eddington accretion is likely responsible for at least some of the ULX population, even when the accretor is a magnetized NS (Bachetti et al. 2014; Mushtukov et al. 2015).

To reproduce observed properties of ULXs, King (2009) estimated a geometric beaming fraction for the X-ray emission, corresponding to the opening solid angle of the accretion funnel, given by

$$f_{b,x} \approx \begin{cases} 0.7, & \dot{m} \ll 10 \\ \frac{73}{\dot{m}^2}, & \dot{m} \gg 10, \end{cases} \quad (4)$$

where the specific constant value of 0.7 in the $\dot{m} \ll 10$ limit is chosen for continuity with the $\dot{m} \gg 10$ limit. Given the requirements of an extremely clean environment to generate an observable FRB (Section 2.4), the relativistic outflow responsible for powering the FRB will itself likely be confined to within a similar solid angle (Figure 1). In such a case, $f_{b,X}$ provides at least a lower limit on the beaming fraction of the FRB itself, f_b , which is defined as the fraction of 4π steradians into which the total power radiated by the FRB is channeled (f_b also denotes the ratio of the angle-integrated to isotropic-equivalent luminosity).

Section 3.3 describes a scenario in which the periodic activity window of FRBs results from precession of the accretion disk's polar funnel (of half-opening angle $\Delta\theta$ and corresponding f_b) across our line of sight (see also Katz 2017, who propose a similar geometry). In this case, taking $f_b = 2\pi(1 - \cos(\Delta\theta))/4\pi \approx \pi(\Delta\theta)^2/(4\pi)$, the duty cycle associated with the FRB activity window is then given by Katz (2021):

$$\zeta \approx \frac{\Delta\theta}{\pi\theta_0} \approx \left(\frac{4f_b}{\pi^2\theta_0^2} \right)^{1/2} \approx \begin{cases} \frac{0.53}{\theta_0}, & \dot{m} \ll 10 \\ \frac{5.4}{\dot{m}\theta_0}, & \dot{m} \gg 10 \end{cases}, \quad (5)$$

where θ_0 is the angle of the axis of precession makes with respect to the observer's line of sight see Figure 1. The observed activity window duty cycle $\zeta \approx 0.3$ – 0.35 of FRB 180916 (Chime/Frb Collaboration et al. 2020), or $\zeta \approx 0.55$ for FRB 121102 (Rajwade et al. 2020), would then imply $\dot{m}\theta_0 \lesssim 10$ (Equation (5) for $\dot{m} \gg 10$). For values $\theta_0 \lesssim 0.1$ – 1 , the implied accretion rates $\dot{m} \gtrsim 10$ – 100 are broadly consistent with those required to power the FRB luminosities from these sources (Figure 2).

2.4. Clean Environment for FRB Escape

A number of physical processes can absorb or attenuate radio waves in the vicinity of an accreting compact object. One of the most severe is induced Compton scattering of the FRB beam by electrons surrounding the source (e.g., Lyubarsky 2008). This makes it highly nontrivial to find the clean environment needed for the FRB to escape to an observer at infinity, given the dense outflows present in super-Eddington accretion systems. The only plausible scenario is for the emission to be generated at large radii, far from the original launching point of the flare (inner magnetosphere), by relativistically expanding material directed outward along the narrow polar accretion funnel. (This funnel, prior to the FRB-generating flare, carried only the comparatively low-density jet, uncontaminated by the mass-loaded disk outflows present at wider angles.)

At the onset of the FRB-generating flare, the polar accretion funnel is filled by the plasma of whatever jet of lower power $L_q = \eta_q L_{BZ}$ was present just prior to the flare, where here $\eta_q \lesssim 1$ is the efficiency of the steady “quiescent” jet relative to that of the higher power $L_{BZ} \sim \eta \dot{M} c^2$ of the transient outburst responsible for powering the FRB (Equation (2)). Below, we discuss different physical interpretations of the low $\eta_q \ll 1$ medium, such as if it truly indicates a less efficient jet (at the same accretion rate, \dot{M}), or just a much lower \dot{M} .

The lab-frame electron density of the quiescent jet at radius r from the compact object is given by

$$n_q = \frac{\eta_q L_{BZ}}{4\pi(1 + \sigma_q) f_b \Gamma_q m_p c^3 r^2}, \quad (6)$$

where σ_q and Γ_q are the magnetization and bulk Lorentz factor of the quiescent jet, respectively, and we have assumed an electron-ion jet composition¹², where m_p is the proton mass.

The optical depth due to induced electron scattering above a radius r in the wind, for an FRB of isotropic-equivalent luminosity L_{FRB} , duration t_{FRB} , and frequency ν_{FRB} , is approximately given by (Lyubarsky 2008; Metzger et al. 2019):

$$\tau_c \sim \frac{3}{320\pi^2} \frac{\sigma_T}{m_e} \frac{L_{FRB} \cdot ct_{FRB} \cdot n_q}{\nu_{FRB}^3 r^2} \cdot \Gamma_q^3, \quad (7)$$

where σ_T is the Thomson cross section, and the factor of Γ_q^3 follows from the relativistic transformation of the induced scattering optical depth from the rest frame of the upstream wind (Margalit et al. 2020).¹³

Substituting Equation (6) with $L_q = \eta_q L_{FRB} f_b / f_\xi$ into Equation (7), we find that $\tau_c \lesssim 1$ is achieved at radii satisfying

$$r \gtrsim r_c \approx \left[\frac{3\sigma_T \eta_q L_{FRB}^2 t_{FRB} \Gamma_q^2}{1280\pi^3 m_e m_p c^2 \nu_{FRB}^3 f_\xi} \right]^{1/4} \\ \approx 8 \times 10^{13} \text{cm} \frac{L_{40}^{1/2} t_{-3}^{1/4} \Gamma_{q,2}^{1/2}}{\nu_9^{3/4} f_{\xi,-3}^{1/4}} \frac{\eta_{q,-3}^{1/4}}{(1 + \sigma_q)^{1/4}}, \quad (8)$$

where $\eta_{q,-3} \equiv \eta_q/(10^{-3})$, $\Gamma_{q,2} = \Gamma_q/100$, $\nu_9 = \nu_{FRB}/10^9 \text{Hz}$, $L_{40} \equiv L_{FRB}/10^{40} \text{erg s}^{-1}$, $t_{-3} \equiv t_{FRB}/1 \text{ms}$, $f_{\xi,-3} \equiv f_\xi/10^{-3}$.

To produce an FRB of duration $t_{FRB} \sim r_{FRB}/(2\Gamma^2 c)$ at radius $r_{FRB} > r_c$, the Lorentz factor Γ of the emitting region must obey

$$\Gamma > \Gamma_{\min} \approx \left(\frac{r_c}{2ct_{FRB}} \right)^{1/2} \approx 400 r_{c,13}^{1/2} t_{-3}^{-1/2}, \quad (9)$$

where $r_{c,13} \equiv r_c/(10^{13} \text{cm})$, and we have assumed a mildly magnetized upstream $\sigma_q \lesssim 1$. The Thomson depth from the emission radius $r_{FRB} > r_c$ through the quiescent outflow at large radii is given by

$$\tau_T \simeq \int_{r_{FRB}}^{\infty} n_q \sigma_T dr \approx \frac{\eta_q L_{BZ} \sigma_T}{4\pi f_b \Gamma_q m_p c^3 r_{FRB} (1 + \sigma_q)} \\ \approx 1.5 \times 10^{-11} \frac{m_\bullet}{r_{FRB}} \frac{r_c}{r_{c,13} f_{b,-1} \Gamma_{q,2} (1 + \sigma_q)}, \quad (10)$$

¹² The composition of a BH or NS jet is likely to be dominated by electron/positron pairs on small scales close to the compact object (e.g., Globus & Levinson 2013). However, by the larger radial scales of interest, the quiescent jet may have entrained baryons from the jet walls defined by the surrounding disk wind.

¹³ An additional complication arises from the impact of the strong wave of the FRB in accelerating the electrons in the upstream scattering medium to relativistic speeds. However, Margalit et al. (2020) show that the enhancement in the optical depth due to this effect is canceled by the suppression of the scattering rate of the relativistic electrons (Lyubarsky 2019).

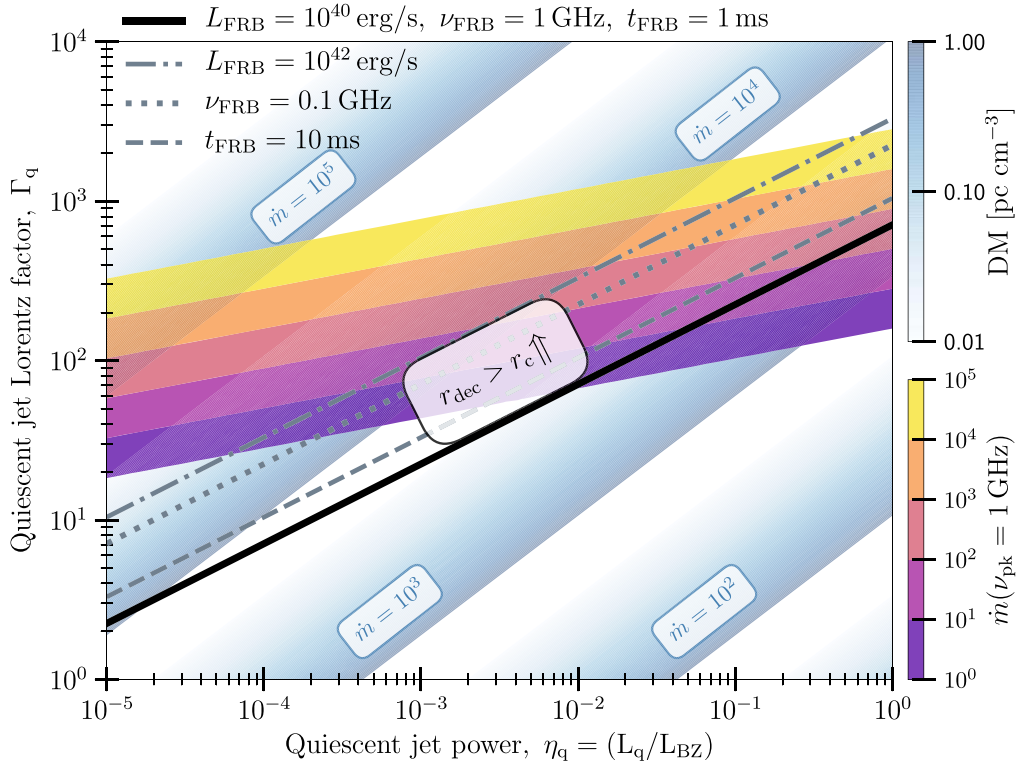


Figure 3. The quiescent jet just prior to the FRB flare must be comparatively dilute and highly relativistic. Here we show the allowed parameter space of the quiescent jet (η_q , Γ_q), based on the constraints from the optical depth for FRB escape, and on the local dispersion measure (DM) variation. The requirement of $r_{\text{dec}} > r_c$ for an optically thin upstream medium is demarcated by the diagonal lines (see Equations (8) and (12)). The solid black line corresponds to the “fiducial FRB” with $L_{\text{FRB}} = 10^{40} \text{ erg s}^{-1}$, $\nu_{\text{FRB}} = 1 \text{ GHz}$, $t_{\text{FRB}} = 1 \text{ ms}$. The gray dashed–dotted, dotted, and dashed lines denote the deviation of the burst luminosity ($L_{\text{FRB}} = 10^{42} \text{ erg s}^{-1}$), frequency ($\nu_{\text{FRB}} = 0.1 \text{ GHz}$), and the duration ($t_{\text{FRB}} = 10 \text{ ms}$), respectively, from the fiducial case. The local environmental contribution to the DM, corresponding to different $\dot{m} \in [10, 10^3]$, is denoted by the fading blue bands (assuming $r_{\text{FRB}} = r_{\text{dec}}$; see Equations (11) and (12)); the dark region corresponds to the expected upper limit of $\sim 1 \text{ pc cm}^{-3}$. The values of η_q and Γ_q required to produce an emission peak at $\nu_{\text{pk}} = 1 \text{ GHz}$, for different $\dot{m} \in [1, 10^5]$, are represented by the central yellow–violet “emission contours” (see Equation (14)). For a given \dot{m} , the allowed range of η_q and Γ_q consists of the regions to the left of the intersection of the corresponding emission contour with the $\text{DM} = 1 \text{ pc cm}^{-3}$ band, and above the $r_{\text{dec}} = r_c$ line. Throughout, we assume $\eta = 1$, $\sigma_q = 1$, $f_\xi = 10^{-3}$, flare duration $t_f \sim t_{\text{min}} = 1 \text{ ms}$, redshift $z = 0$, $f_b \approx 70/\dot{m}^2$, and $m_* = 10$.

and the corresponding DM,

$$\begin{aligned} \text{DM}[\text{pc cm}^{-3}] &\simeq 5 \times 10^5 \frac{\tau_T \Gamma_q}{(1+z)} \\ &\simeq \frac{10^{-3}}{(1+z)} \frac{r_c}{r_{\text{FRB}}} \frac{m_*}{10} \frac{\eta \dot{m}}{r_{c,13f_b,-1}} \frac{\eta_{q,-3}}{(1+\sigma_q)}, \end{aligned} \quad (11)$$

where z is the source redshift, and the factor Γ_q arises from the Lorentz transformation of the measured DM.

In addition to requiring an FRB be freely able to propagate to Earth ($\tau_c < 1$), one must also not overproduce the measured local DM value or its time variation between bursts from the same source, ΔDM (for example, $\Delta\text{DM} \lesssim 2 \text{ pc cm}^{-3}$ in FRB 180916; Chime/Frb Collaboration et al. 2020). Equations (8)–(11) reveal that satisfying both of these conditions is possible, but it requires (1) the FRB to be generated by a highly relativistic outflow, $\Gamma \gg 100$, (2) which propagates into the medium corresponding to a jet of extremely low luminosity, $\eta_q \ll 10^{-2}$ and/or one with a very high magnetization $\sigma_q \gg 1$. The next section describes how similar requirements emerge within a specific FRB emission model. Figure 3 summarizes the allowed parameter space of quiescent jet properties needed to simultaneously satisfy constraints on the shock emission radius ($r_{\text{dec}} > r_c$) and on the lack of local time-variable DM contribution due to propagation through the jet.

Can accreting stellar-mass compact objects generate outflows with $\Gamma > 100$? The jets of Galactic X-ray binaries achieve Lorentz factors of at least a few to tens (e.g., Mirabel & Rodríguez 1994; Fender et al. 2004), although the constraints are model dependent and generally amount to lower limits (Miller-Jones et al. 2006). As in jets from active galactic nuclei (AGNs), radiative acceleration of optically thin gas to relativistic velocities is severely limited by radiation drag effects (e.g., Phinney 1982); however, these effects are mitigated if the flow entrains enough matter to shield itself. From radiation acceleration alone, Begelman (2014) argue that jets from super-Eddington accretion systems can achieve $\Gamma \simeq \dot{m}^{1/4}$, corresponding to $\Gamma \gtrsim 5$ for $\dot{m} \gtrsim 10^3$. Even higher Lorentz factors can be achieved by acceleration resulting from magnetic dissipation of a high- σ flow in an optically thick environment (e.g., Drenkhahn & Spruit 2002), and impulsively due to magnetic pressure gradients within the ejecta (Granot et al. 2011). For example, an extreme limit is gamma-ray burst jets, which attain $\Gamma \gtrsim 100$ –1000 (e.g., Lithwick & Sari 2001). Taken together, it cannot be excluded that highly super-Eddington systems—unlike the majority of X-ray binaries in our Galaxy—are capable for brief periods of generating outflows that satisfy the constraints (9) and (11).

We also require a low effective efficiency $\eta_q \ll 1$, and/or large magnetization $\sigma_q \gg 1$, in the quiescent jet. A large contrast in jet power between the quiescent and an FRB-generating

flaring state would be generated by a sudden (\sim dynamical-timescale) large increase in the mass accretion rate reaching the central object. This could be achieved, for example, by a highly magnetized NS accretor transitioning between a state of steady accretion and a “propeller” regime in which accretion is prohibited (e.g., Parfrey & Tchekhovskoy 2017). Although changes in the accretion rate up to a factor $\sim 10^3$ are indeed observed in Galactic X-ray pulsars (Tsygankov et al. 2016), the frequency of mode-switching would need to be much more rapid than observed to explain many recurring FRBs, which exhibit inter-burst intervals as short as ~ 10 – 100 s (e.g., Gourdji et al. 2019). Large amplitude changes in the accretion rate (factor of $\sim 10^3$) are also inferred in ULXs (Kaaret & Feng 2009; Bachetti et al. 2014) and from the class of low-mass X-ray binaries known as soft X-ray transients (e.g., Tanaka & Shibazaki 1996), but again over timescales much longer than needed to explain many FRB sources.

Even for a constant accretion rate \dot{M}_* , an abrupt rise in the jet efficiency $\eta \propto \Phi_B^2$ can be driven by an increase in the magnetic flux Φ_B threading the BH horizon. Although one has $\eta = \eta_q = \mathcal{O}(1)$ for the jet of a spinning BH in a persistently MAD state (Tchekhovskoy et al. 2010), long phases of $\eta_q \ll 1$ are possible if the inner disk only irregularly receives a large magnetic flux bundle (Spruit & Uzdensky 2005; Parfrey et al. 2015).

Finally, the above constraints are also satisfied even for a relatively constant jet power ($\eta_q \sim 1$) if the quiescent jet is extremely highly magnetized $\sigma_q \gg 1$ (and hence is low density) relative to the FRB-generating flare. However, in our calculations that follow, we focus on the case of moderate upstream magnetization and a large contrast between the flaring and quiescent jet luminosities.

2.5. Emission Mechanism

Advancing beyond the basic considerations of the previous section requires identifying a specific mechanism to convert a sudden release of relativistic energy from the engine (“flare”) into coherent radio emission at radii $r_{\text{FRB}} \gg r_c \sim 10^{13}$ cm. One such emission mechanism, which we focus on for concreteness, is synchrotron maser emission from the relativistic shock generated as flare ejecta from the central engine collide with a magnetized upstream (Lyubarsky 2014; Beloborodov 2017; Metzger et al. 2019; see also Waxman 2017). In the present context, the upstream medium is the quiescent jet from earlier epochs.

Fast magnetosonic waves produced by plasmoid mergers in magnetic reconnection, which occur in the current sheets of BH magnetospheres (e.g., Philippov et al. 2019; Lyubarsky 2020), or induced reconnection in the striped high- σ_q quiescent jet (and resulting inverse turbulent cascade; Zrake & Arons 2017), provide an alternative emission mechanism for the flare. However, the conditions for an FRB to escape from the magnetic reconnection-induced relativistically hot plasma are generally more severe than from a cold upstream (Lyubarsky 2008).

Returning to the shock scenario, we consider an accretion flare, which releases a transient ultra-relativistic outflow of power $L_f \sim \eta \dot{M}_* c^2$ (Equation (2)), duration $t_f \sim t_{\text{min}}$ (Equation (1)), and radial bulk Lorentz factor $\Gamma_f \gg \Gamma_{\text{min}}, \Gamma_q$. Such flare ejecta could represent a magnetized plasmoid generated by a powerful reconnection event close to the BH/NS magnetosphere or light cylinder (e.g., Parfrey et al. 2015; Ripperda et al. 2019; Yuan et al.

2020). The flare ejecta (with initial Lorentz factor Γ) will sweep up gas in the pre-existing quiescent jet (Equation (6)), generating a forward shock by a radius (Sari & Piran 1995)

$$r_{\text{dec}} \approx 2\Gamma_{\text{sh}}^2 c \cdot t_f \approx 2 \times 10^{13} \eta_{q,-3}^{-1/2} t_{f,-3} \Gamma_{q,2}^2 \text{ cm}, \quad (12)$$

where (Beloborodov 2017)

$$\Gamma_{\text{sh}} \approx \Gamma_q \left(\frac{L_f}{L_q} \right)^{1/4} \simeq \frac{\Gamma_q}{\eta_q^{1/4}} \approx 560 \frac{\Gamma_{q,2}}{\eta_{q,-3}^{1/4}}, \quad (13)$$

is the Lorentz factor of the shocked gas during the initial deceleration phase. As discussed above, for the deceleration—and concomitant radio emission—to occur in an optically thin environment ($r_{\text{dec}} \gg r_c$; Equation (8)), we require a large quiescent jet Lorentz factor $\Gamma_q \gtrsim 100$ and/or a large contrast $\eta_q \lesssim 10^{-3}$, between the jet luminosity during the flare and that of prior quiescent state (Figure 3).

The synchrotron maser emission peaks at an electromagnetic frequency (e.g., Gallant et al. 1992; Plotnikov & Sironi 2019)

$$\begin{aligned} \nu_{\text{pk}} &\sim \frac{3\Gamma_{\text{sh}} c}{2\pi r_L} \sim \frac{3e\sigma_q^{1/2} (L_f L_q)^{1/4}}{2\pi m_e c^{3/2} r_{\text{FRB}}} \\ &\approx \frac{e\eta^{1/2} \sigma_q^{1/2} L_{\text{Edd}}^{1/2} r_{\text{dec}}}{4\pi m_e c^{5/2} r_{\text{FRB}}} \frac{\dot{m}^{1/2} \eta_q^{3/4}}{t_f \Gamma_q^2} \\ &\approx 1.9 \text{ GHz} \left(\frac{r_{\text{FRB}}}{r_{\text{dec}}} \right)^{-1} \left(\frac{\dot{m}_*}{10} \right)^{1/2} \left(\frac{\dot{m}}{10^2} \right)^{1/2} \frac{\eta^{1/2} \eta_{q,-3}^{3/4} \sigma_q^{1/2}}{\Gamma_{q,2}^2 t_{-3}}, \end{aligned} \quad (14)$$

where $r_L = \Gamma_q m_e c^2 / e B_q$ is the Larmor radius of electrons in the shocked plasma, $B_q \simeq (L_q \sigma_q / c r_{\text{FRB}}^2)^{1/2}$ is the upstream lab-frame magnetic field of the quiescent jet material at the radius r_{FRB} of the FRB emission assuming $\sigma_q \gtrsim 1$. The efficiency of the FRB maser emission is $f_\xi \sim 10^{-3}$ for $\sigma_q \gtrsim 1$ (Plotnikov & Sironi 2019; Babul & Sironi 2020), motivating the choice for $L_{\text{FRB}}^{\text{max}}$ in Figure 2. Colored lines in Figure 3 show the quiescent jet properties required to produce a burst of frequency $\nu_{\text{pk}} \sim 1$ GHz for different values of \dot{m} .

As described previously in the context of other central-engine models, deceleration of the flare ejecta by the blast wave and its propagation to lower densities at radii $\gtrsim r_{\text{dec}}$ produces downward drifting of ν_{pk} and hence the frequency structure of the bursts (Beloborodov 2020; Margalit et al. 2019; Metzger et al. 2019; Sridhar et al. 2021), similar to that observed in the sub-bursts of FRB 121102 (Hessels et al. 2019) and the CHIME repeaters (CHIME/FRB Collaboration et al. 2019).¹⁴ For $\sigma_q \gg 1$, the bursts are predicted to be nearly 100% linearly polarized at the source, dominated by the so-called “X-mode” waves. These waves have their electric field perpendicular to the upstream magnetic field, and hence also for a laminar quiescent jet that is parallel to the approximately fixed direction of the BH/NS spin vector. However, for lower $\sigma_q \lesssim 1$, the shock also radiates an intense “O-mode”, with power nearly

¹⁴ The downward drifting of ν_{pk} , and the burst substructures, are also possible for a radially decreasing upstream density profile (e.g., the case of inspiral winds during NS mergers; Sridhar et al. 2021), and due to the nonlinear propagation effects of FRBs (e.g., self-modulation; Sobacchi et al. 2021), respectively.

comparable to the X-mode, which then deteriorates the polarization degree (Iwamoto et al. 2018).

A roughly constant polarization angle over many distinct bursts is consistent with observations of FRB 121102 (e.g., Michilli et al. 2018) but in tension with other bursts that show polarization swings across the burst duration (e.g., Luo et al. 2020; Day et al. 2020). The latter require a more complicated magnetic field geometry in the upstream jet material than a laminar jet, for instance due to the effects of kink instabilities (e.g., Bromberg & Tchekhovskoy 2016) or the interaction of the jet with the accretion disk wind at large radii as a result of disk precession (Section 2.4).

3. Binary Properties

The majority of accreting Galactic NS/BH sources reside in long-lived X-ray binary systems with mass-transfer rates at or below the Eddington rate. However, as shown in Figure 2, such sources are energetically strained to explain most luminous FRBs. Nevertheless, there exist more extreme systems with much higher accretion rates. These include the microquasar binary SS433 (Margon 1984; Fabrika 2004), which is likely a BH being fed by a massive late A-type companion star at a super-Eddington rate (e.g., Hillwig & Gies 2008). Such a source viewed face-on would be a strong (and periodic due to jet precession) X-ray source akin to a ULX.¹⁵

One binary channel capable of generating sustained levels of highly super-Eddington accretion is stable thermal-timescale mass transfer. This can occur as an evolved massive secondary star undergoes Roche Lobe overflow, either on the main sequence or later when crossing the Hertzsprung gap to become a giant (e.g., King & Begelman 1999; King et al. 2001; Rappaport et al. 2005; Wiktorowicz et al. 2015). As the stellar envelope becomes fully convective approaching the Hayashi track, the adiabatic response of the star to mass loss can lead to dynamically unstable mass transfer, which manifests as a “common envelope event” engulfing the system in gas and ultimately precluding the clean environment necessary for FRB formation. However, as emphasized by Marchant et al. (2017) and Pavlovskii et al. (2017), a large fraction of systems nominally in the unstable regime may in fact undergo stable mass transfer due to their outermost surface layers remaining radiative.¹⁶

This section considers whether such systems provide the accreting BH/NS systems required to power FRBs as discussed thus far. We initially focus on stable mass-transfer systems, and, finding it possibly insufficient to account for the most luminous FRBs, we return to the shorter-lived unstable systems at the end.

3.1. Mass-transfer Rate

For thermal-timescale mass transfer from a star of mass $M_* = m_* M_\odot$ in a semidetached binary to the companion of mass m_* (in our case, a BH or NS), the mass-transfer rate can

achieve a value (e.g., Kolb 1998),

$$\dot{M}_{\text{tr}} \sim \frac{M_*}{\tau_{\text{KH}}} \sim 3 \times 10^{-8} m_*^{2.6} M_\odot \text{yr}^{-1}, \quad (15)$$

where

$$\tau_{\text{KH}} \approx 3 \times 10^7 \frac{m_*^2}{r_* l_*} \text{yr} \approx 3 \times 10^7 m_*^{-1.6} \text{yr} \quad (16)$$

is the Kelvin–Helmholtz time of the star when it leaves the main sequence, and $L_* = l_* L_\odot$ is its luminosity. In the final equalities, we have assumed a main-sequence star of mass $1 \lesssim m_* \lesssim 40$ with a radiative envelope, for which $r_* \propto m_*^{0.6}$ and $l_* \propto m_*^3$.

On the other hand, \dot{M}_{tr} cannot be arbitrarily large, or the super-Eddington disk cannot “fit” into the binary. More precisely, if the disk is locally super-Eddington even at the circularization radius, then a thick disk encompasses the entire system and common envelope-like runaway will still occur. King & Begelman (1999) estimated this occurs for $m_* \gtrsim 53 m_\star^{0.18}$, placing an Eddington-scaled upper limit on \dot{M}_{tr} of

$$\frac{\dot{M}_{\text{tr}}^{\text{max}}}{\dot{M}_{\text{Edd}}} \sim 1.2 \times 10^5 \left(\frac{m_*}{10} \right)^{-0.53}. \quad (17)$$

To power FRB emission, we are interested in the accretion rate reaching the innermost radii of the disk. However, for super-Eddington accretion, only a small fraction of the transferred mass is expected to reach the BH due to massive winds (e.g., Blandford & Begelman 1999). In particular, for $\dot{M}_{\text{tr}} \lesssim \dot{M}_{\text{tr}}^{\text{max}}$, we expect

$$\dot{M} \simeq \dot{M}_{\text{tr}} \left(\frac{R_{\text{Edd}}}{R_{\text{isco}}} \right)^{-p}, \quad (18)$$

where $R_{\text{Edd}} \simeq R_g \left(\frac{\dot{M}_{\text{tr}}}{\dot{M}_{\text{Edd}}} \right)$ is the trapping radius interior to which the disk becomes locally super-Eddington and $0 < p < 1$. Taking a value $p \approx 0.7$ motivated by hydrodynamical simulations of RIAFs (Yuan & Narayan 2014), we obtain

$$\dot{m} = \left(\frac{R_{\text{isco}}}{R_g} \right)^{0.7} \left(\frac{\dot{M}_{\text{tr}}}{\dot{M}_{\text{Edd}}} \right)^{0.3}. \quad (19)$$

The upper limit on the mass-transfer rate (17) then becomes an upper limit on the accretion rate reaching the central compact object,

$$\dot{m} \lesssim 54 \left(\frac{R_{\text{isco}}}{2R_g} \right)^{0.7} \left(\frac{m_*}{10} \right)^{-0.16}. \quad (20)$$

From Equation (3), we obtain a theoretical maximum of the isotropic-equivalent FRB luminosity for stably accreting sources:

$$L_{\text{FRB,mt}}^{\text{max}} \approx 2.2 L_{\text{Edd}} f_{\xi,-3} \left(\frac{R_{\text{isco}}}{2R_g} \right)^{2.1} \left(\frac{m_*}{10} \right)^{-0.53}, \quad (21)$$

where we have taken $f_b = f_{b,x}$ (Equation (4)) in the $\dot{m} \gg 10$ limit (as satisfied for $m_* \lesssim 10^3$ for $R_{\text{isco}} \sim R_g$).

The constraint (21) is shown as a black line in Figure 2. Many observed FRBs can in principle satisfy the $L_{\text{FRB,mt}}^{\text{max}}$ limit. However, it is violated by the most luminous sources,

¹⁵ SS433 in fact exhibits X-ray emission with evidence for precession in the light curve (Atapin & Fabrika 2016), which are believed to arise from the jet rather than the accretion disk.

¹⁶ Making such systems stable also reduces the predicted rate of binary BH mergers from population synthesis models, bringing them into better accord with observations by LIGO/Virgo.

particularly many (currently) non-repeating sources. These FRBs could still be powered by accreting systems if the latter are undergoing *unstable* mass transfer at a rate $\dot{M}_{\text{tr}} \gg \dot{M}_{\text{tr, max}}$. Such systems have just begun mass transfer but are in the process of evolving toward a merger or common envelope (e.g., MacLeod & Loeb 2020).

The lifetime of unstable systems as FRB sources corresponds to the timescale for runaway accretion. Based on observations and modeling of the stellar merger V1309 Sco (Tylanda et al. 2011; Pejcha 2014; Pejcha et al. 2017), this evolution time can be estimated as¹⁷

$$\tau_{\text{unst}} \sim (5-100)P_{\text{orb}} \sim (10 - 10^5)\text{d}, \quad (22)$$

where $P_{\text{orb}} \sim 1-1000$ d is the binary orbital period (Equation (26)). The resulting mass-transfer rate, $\dot{M}_{\text{tr}} \sim M_*/\tau_{\text{unst}} \sim 10^3-10^7 \dot{M}_{\text{Edd}}$ (e.g., for $M_* \sim 10M_{\odot}$), can in principle exceed $\dot{M}_{\text{tr}}^{\text{max}}$ (Equation (17)) by orders of magnitude. Even with accounting for mass loss from disk winds, this results in accretion rates reaching the compact object $\dot{m} \gtrsim 100$ (Equation (19)), sufficient to explain the most luminous FRB sources (Figure 2). As the merger proceeds, the accretion rate rises exponentially, and the nature of the gaseous environment surrounding the binary will become increasingly “messy.” This will eventually lead to a cessation of FRB activity, at the very latest once the compact object plunges into the donor star or is completely engulfed by the common envelope on the timescale $\sim \tau_{\text{unst}}$.

If a system undergoing unstable accretion were to generate multiple FRBs, the “runaway” process should impart a systematic variation in the FRB properties approaching the dynamical plunge. For example, as the accretion rate rises—and the opening angle of the accretion funnel shrinks—the isotropic-equivalent luminosity of the bursts could increase in time, at least initially.

3.2. Source Rates

Under the assumption that all FRBs repeat with a luminosity function similar to the repeat bursts from FRB 121102, Nicholl et al. (2017) placed a constraint on the volumetric space density of FRB sources, \mathcal{N}_{FRB} (see also Lu & Kumar 2016). The latter can be expressed as the product of the FRB source formation rate \mathcal{R} and the average active lifetime τ , viz.

$$\mathcal{N}_{\text{FRB}} = \mathcal{R} \cdot \tau \sim 1.3 \times 10^4 \left(\frac{f_b}{0.1} \right)^{-1} \left(\frac{\zeta}{0.1} \right)^{-1} \text{Gpc}^{-3}, \quad (23)$$

where f_b and ζ are the average beaming fraction of each FRB and the duty cycle of the active window, respectively (which may be related by the common geometry of the accretion funnel; Section 3.3).

One relevant comparison is to the volumetric rate of ULX sources. The local rate of all ULXs (defined by X-ray luminosities $L_X > 10^{39} \text{erg s}^{-1}$) is $\mathcal{N}_{\text{ULX},39} \sim 2 \times 10^7 \text{Gpc}^{-3}$ (Swartz et al. 2011). However, the luminosity function steeply decreases moving to the higher isotropic-equivalent luminosities ($> L_X \sim 10^{40} \text{erg s}^{-1}$) required in our scenario to power FRBs, exhibiting a sharp break above $L_X \sim 10^{40} \text{erg s}^{-1}$, such that the rate above $L_X \sim 10^{41} \text{erg s}^{-1}$ is $\mathcal{N}_{\text{ULX},41} \sim 10^4 \text{Gpc}^{-3}$ (Mineo et al. 2012). Yet more luminous ULXs with

$L_X \gtrsim 10^{42} \text{erg s}^{-1}$, such as the “hyper-luminous” source HLX-1 (Farrell et al. 2009), are even less common (Gao et al. 2003).

For stably accreting systems, the maximum FRB active lifetime is of the order of the Kelvin–Helmholtz time, τ_{KH} (Equation (16)). Accounting for the bulk of the FRB population through this channel ($\tau = \tau_{\text{KH}}$ in Equation (23)) then requires a source formation rate

$$\mathcal{R}_{\text{stable}} \sim 0.02 \left(\frac{m_*}{10} \right)^{1.6} \left(\frac{f_b}{0.1} \right)^{-1} \left(\frac{\zeta}{0.1} \right)^{-1} \text{Gpc}^{-3} \text{yr}^{-1}. \quad (24)$$

Pavlovskii et al. (2017) estimate a Milky Way formation rate of $\sim 3 \times 10^{-5} \text{yr}^{-1}$ binaries with mass-transfer rates $\dot{M}_{\text{tr}} \gtrsim 100 \dot{M}_{\text{Edd}}$, corresponding roughly to $\mathcal{R} \sim 100 \text{Gpc}^{-3} \text{yr}^{-1}$. The rate is higher in subsolar metallicity environments (Section 4.1). Thus, only a small fraction $\lesssim 10^{-3}$ of potentially stable super-Eddington systems need to serve as active FRB sources. This suggests an extra variable would need to be responsible for making a small fraction of ULX binaries into FRB sources.

Several special conditions may indeed need to be met to produce an observable FRB (Section 2.5). For example, generating a flare of sufficient power may require a large magnetic flux threading the BH, a task aided if the mass-transferring star is itself highly magnetized. Although strongly magnetized massive stars are relatively common (e.g., the magnetic A-stars, with a 10% occurrence rate), very few magnetic stars are in binaries (see Shultz et al. 2015 for an exception). This low binary fraction could be explained if strong magnetic fields are the result of stellar mergers (e.g., Schneider et al. 2019). In such a case, forming a mass-transferring binary with a magnetized secondary might require a low-probability scenario, such as chaotic evolution or Kozai–Lidov oscillations in an initial hierarchical triple or quadrupole system (which acts to bring a magnetized stellar merger product into contact with the NS/BH primary).

The most luminous FRB sources require the high accretion rates achieved by binary systems undergoing unstable mass transfer just prior to merging or entering a common envelope phase. Applying the shorter lifetime of unstable systems, $\tau_{\text{unst}} \ll \tau_{\text{KH}}$ (Equation (22)) to Equation (23), leads to a higher required rate of unstable events:

$$\begin{aligned} \mathcal{R}_{\text{unst}} &\sim 5 \times 10^3 \left(\frac{f_{\text{unst}}}{0.1} \right) \left(\frac{\tau_{\text{unst}}}{100 P_{\text{orb}}} \right)^{-1} \left(\frac{P_{\text{orb}}}{10 \text{d}} \right)^{-1} \\ &\times \left(\frac{f_b}{0.01} \right)^{-1} \left(\frac{\zeta}{0.1} \right)^{-1} \text{Gpc}^{-3} \text{yr}^{-1}, \end{aligned} \quad (25)$$

where f_{unst} is the fraction of FRBs that arise from unstably accreting systems, and we have scaled f_b to the smaller value expected for $\dot{m} \gg 10$ (Equation (4)).

It is useful to compare the rate of Equation (25) to that of luminous red novae (LRNs), optical transients from stellar mergers triggered by unstable mass transfer (Soker & Tylanda 2006; Tylanda et al. 2011). The most luminous LRNs, which arise from the merger of massive stars $\gtrsim 10M_{\odot}$, occur at a rate of $\mathcal{R}_{\text{LRN}} \sim 10^5 \text{Gpc}^{-3} \text{yr}^{-1}$ (Kochanek et al. 2014). Although the merging systems of harboring BH/NS primaries of interest are even rarer than ordinary massive star mergers, their rates may still be consistent with the most luminous FRBs arising from unstable binaries.

¹⁷ In the luminous red nova AT 2018bwo, Blagorodnova et al. (2021) inferred that a state of thermal-timescale unstable mass transfer was maintained for nearly a decade prior to evolving toward a common envelope.

3.3. Periodicity

The bursts from FRB 180916 and 121102 arrive in a consistent phase window associated with a period of $\approx 16.35 \pm 0.15$ d and 161 ± 5 d, respectively (Chime/Frb Collaboration et al. 2020; Rajwade et al. 2020; Cruces et al. 2021). In previous scenarios attributing FRBs to NS activity in a binary, this periodicity was proposed to result from free-free absorption by the companion star wind (e.g., Lyutikov et al. 2020). However, such a scenario predicts a narrower observing window at lower radio frequencies, in tension with observations of FRB 180916 (Pastor-Marazuela et al. 2020; Pleunis et al. 2021). By contrast, in the super-Eddington accretion scenario presented here, a more natural explanation arises from geometric beaming by the narrow clean funnel as the BH jet crosses the observer line of sight (Figure 1; see also Katz 2017).

Two timescales naturally arise in association with a binary, that of orbital motion and that due to disk/jet precession. An orbital period could manifest in the window of FRB activity in the case of a mildly eccentric binary in which mass transfer is maximal during pericenter passage. For a semidetached binary of mass ratio $q \equiv M_*/M_*$, the orbital period is related to the mean density of the mass-transferring star $\bar{\rho}_*$ according to Paczyński (1971)

$$P_{\text{orb}} \simeq 0.35 \text{ d} \left(\frac{2}{1+q} \right)^{0.2} \left(\frac{\bar{\rho}_*}{\bar{\rho}_\odot} \right)^{-1/2} \quad (26)$$

$$q \approx 10.88 \text{ d} \left(\frac{m_*}{10} \right)^{0.4} \left(\frac{R_*}{R_*^{\text{MS}}} \right)^{3/2},$$

where in the final line we have scaled the stellar radius R_* to its main-sequence value ($r_* \propto m_*^{0.6}$; $\bar{\rho}_* \approx m_*/r_*^3 \approx m_*^{-0.8}$). To reach the observed periods of tens or hundreds of days, the companion star would need to be evolved off the main sequence, consistent with the mass-transfer scenarios outlined in Section 3.1, for which $R_* \sim (1 - 100)R_*^{\text{MS}}$ (Pavlovskii et al. 2017).

Another source of periodicity can arise due to precession of the accretion funnel along which the FRB is beamed (see Section 2.3, and Figures 1 and 5). If the spin axis of the accreting BH or NS is misaligned with the angular momentum axis of the disk, then the Lens-Thirring (LT) torque applied by the rotating spacetime on the disk may cause the latter to precess (e.g., Middleton et al. 2019). Numerical simulations have shown that for thick disks (with vertical aspect ratio $h/r \gtrsim 0.05$ and low effective α viscosity), the warp propagation timescale is shorter than the differential precession timescale, thereby allowing them to precess as rigid bodies with negligible warping (Fragner & Nelson 2010). The LT precession time in this case is roughly given by (e.g., Fragile et al. 2007; Stone & Loeb 2012)

$$P_{\text{LT}} \approx \frac{\pi G M_* (1 + 2\xi)}{c^3 (5 - 2\xi)} \frac{R_{\text{out}}^{5/2-\xi} R_{\text{in}}^{1/2+\xi}}{R_g^3 a}, \quad (27)$$

where a is the dimensionless BH spin, and $\Sigma \propto r^{-\xi}$ is the surface density of the disk extending from the inner radius $R_{\text{in}} \sim R_{\text{isco}}^{\text{18}}$ to an outer radius $R_{\text{out}} \gg R_{\text{isco}}$. For RIAFs, $\Sigma \propto r^{p-1/2}$ (e.g., Blandford & Begelman 1999), such that for

$p = 0.7$, we have $\xi = -0.2$. On the other hand, $p = 0$ (i.e., $\xi = 0.5$) when all of the mass transferred from the companion star reaches the BH ($\dot{M}_{\text{tr}} = \dot{M}_*$; see 18). The precise load of the outflow is uncertain ($0 < p < 0.7$), and considering its limits, Equation (27) becomes,

$$P_{\text{LT}} \approx \begin{cases} \frac{\pi}{9a} \frac{R_g}{c} \left(\frac{R_{\text{out}}}{R_g} \right)^{2.7} \left(\frac{R_{\text{isco}}}{R_g} \right)^{0.3}, & p = 0.7 \\ \frac{7\pi}{8a} \frac{R_g}{c} \left(\frac{R_{\text{out}}}{R_g} \right)^2 \left(\frac{R_{\text{isco}}}{R_g} \right), & p = 0.0 \end{cases} \quad (28)$$

Taking the outer edge of the disk $R_{\text{out}} \approx R_{\text{RLOF}}/3$ close to the circularization radius (Frank et al. 2002), where (for $0.1 \lesssim q \lesssim 0.8$), we have (Paczynski 1971)

$$\frac{R_{\text{RLOF}}}{a} \simeq 0.462 \left(\frac{q}{1+q} \right)^{1/3}, \quad (29)$$

where a is the binary semimajor axis. Using Kepler's second law, $P_{\text{orb}} = 2\pi [a^3/GM_*(1+q)]^{1/2}$, Equation (28) becomes

$$P_{\text{LT}} \approx \begin{cases} 2.8 \times 10^3 \text{ d} \frac{(q_{1.0} P_{\text{orb}}^2)^{0.9}}{a_{0.9} (m_*/10)^{0.8}}, & p = 0.7 \\ 17 \text{ d} \frac{(q_{1.0} P_{\text{orb}}^2)^{2/3}}{a_{0.9} (m_*/10)^{1/3}}, & p = 0.0 \end{cases} \quad (30)$$

Depending on the BH spin, mass, and mass ratios, precession timescales of tens to thousands of days are possible even from binaries with orbital periods of days (Figure 4). A similar model was proposed to explain the 164 d jet precession timescale of SS433 (Sarazin et al. 1980; Katz 1981). Super-orbital periods in the range of tens of days to 100 d, which could be attributed to precession¹⁹, have been observed in several ULXs (e.g., Mioduszewski et al. 2004; Grisé et al. 2013; Atapin & Fabrika 2016; Luangtip et al. 2016; Brightman et al. 2019, 2020; Vasilopoulos et al. 2020; see Weng & Feng 2018 for a systematic search with Swift observatory).

Observations of the periodic repeater, FRB 180916, reveal that the burst activity window (duty cycle; see Equation (5)) is narrower, and peaks earlier in phase, at higher radio frequencies (Pastor-Marazuela et al. 2020). Furthermore, the low-frequency bursts observed exhibit greater average fluences (Pastor-Marazuela et al. 2020; Pleunis et al. 2021). In the synchrotron maser scenario (Section 2.5), the frequency of the radio emission scales with the properties of the FRB-generating transient flare and the pre-existing quiescent jet as (Equation (14); $L_f \propto \eta$),

$$\nu_{\text{pk}} \propto \frac{L_q^{3/4} \sigma_q^{1/2}}{\Gamma_q^2 L_f^{1/4}}. \quad (31)$$

Thus, if the quiescent jet is “structured” in angle θ measured relative to the jet axis, with both L_q and Γ_q growing toward the jet edge (with Γ_q growing faster), then lower-frequency bursts would be preferentially observed at phases near the edges of the observing window (see Figures 1 and 5). Motivating such a structure, MHD simulations of relativistic magnetized jets find that the jet Poynting flux is concentrated in a hollow cone around the jet core (e.g., Tchekhovskoy et al. 2008). In

¹⁸ Recent works by Sridhar et al. (2019, 2020) and Connors et al. (2020, 2021) have tracked the inner accretion flow properties of microquasars across the bright, ballistic jet-emitting states during an X-ray outburst with state-of-the-art X-ray reflection models, and have demonstrated that the inner edge of the accretion disk extends to $R_{\text{in}} \sim R_{\text{isco}}$ at these states.

¹⁹ Classical mechanisms including Newtonian precession were one of the initial interpretations of the observed super-orbital modulation (Katz 1973; Levine & Jernigan 1982; Katz et al. 1982).

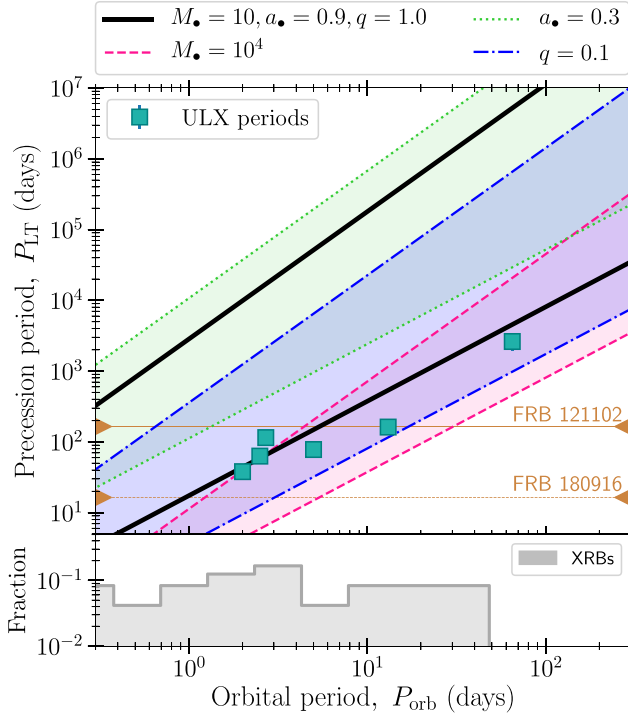


Figure 4. Top panel: the relationship between the BH-companion star orbital period (P_{orb}) and the LT precession period (P_{LT}) of an inner thick accretion disk. The band covered between the solid black lines represents the range of P_{LT} values for a fiducial case: $M_* = 10M_\odot$, $a_* = 0.9$, $q = 1.0$. The upper and lower limits of $P_{\text{LT}}(P_{\text{orb}})$ are set by the nature of the disk outflows—RIAF-like and negligible outflow—parameterized by $p = 0.7$ and $p = 0$, respectively (see Equations (18) and (30)). The region covered between the green (dotted), blue (dashed-dotted), and pink (dashed) bands denotes the independent variation of a_* ($= 0.3$), q ($= 0.1$), and M_* ($= 10^4 M_\odot$), respectively, from the fiducial case. The observed ~ 160 d periodicity in FRB 121102 and the ~ 16 d periodicity in FRB 180916—corresponding to P_{LT} in the paradigm presented here—are denoted by brown horizontal lines connecting the left and right facing triangles. The green squares denote the periodicities observed in ULXs, where we interpret the observed super-orbital periods as P_{LT} . The represented ULXs are: NGC 7793 P13 (Motch et al. 2014), SS 433 (Abell & Margon 1979), M82 X-2 (Bachetti et al. 2014; Brightman et al. 2019), M51 ULX-7 (Rodríguez Castillo et al. 2020; Brightman et al. 2020), NGC 5907 ULX-1 (Walton et al. 2016; Israel et al. 2017), and NGC 5408 X-1 (Grisé et al. 2013). Bottom panel: the distribution of orbital periods of bright Galactic X-ray binaries ($L_X > 10^{38} \text{ erg s}^{-1}$; gray) obtained from the WATCHDOG catalog (Tetarenko et al. 2016).

addition, the efficiency of the synchrotron maser emission depends on the magnetization of the upstream medium (Plotnikov & Sironi 2019); thus, angular structure in the magnetization of the quiescent jet $\sigma_q(\theta)$ would also imprint systematic variations in burst luminosity across the observing window (and hence with radio frequency; see Figure 1).

Regarding the lag in the central phase of FRB activity with radio frequency (Pastor-Marazuela et al. 2020), we speculate that it results from the curvature of quiescent jet cavity due to the effect of precession-driven motion of the disk winds (see Section 4.2). Even if the FRB-emitting flare ejecta is launched ballistically outwards along the axis defined by the instantaneous base of the jet, by the radii of emission $\gtrsim r_{\text{dec}} \sim 10^{14} \text{ cm}$ (Equation (12)), the quiescent jet medium into which the shock propagates could exhibit asymmetry between the leading and trailing edges of the precession cone, as the wind shaping the jet cavity walls is dragged back against the direction of precession. Furthermore, the properties of the curved quiescent

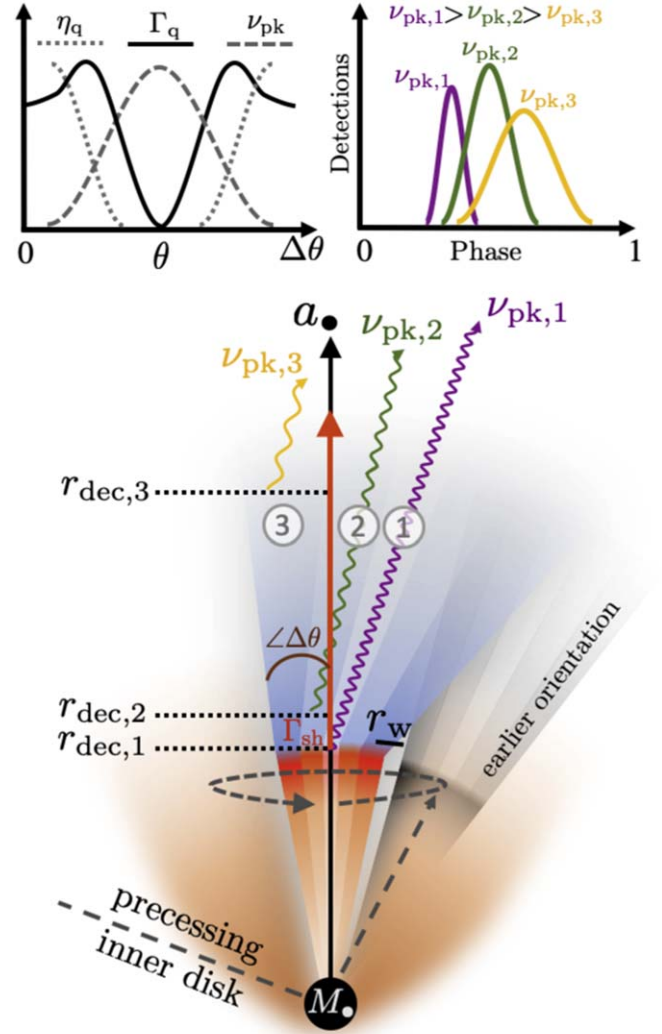


Figure 5. A curved quiescent jet cavity (blue bands) is bent toward its earlier orientation (gray cone) due to the drag of the precessing disk winds (brown) at a scale of r_w (Equation (33)). The FRB-emitting flaring ejecta (red bands) are launched along the instantaneous jet axis (red vertical line with arrow), and propagate into an asymmetric (spirally curved) upstream medium. The radio frequency of the burst depends on whether the flare interacts with the core or sheath of the quiescent jet. The varying properties of the quiescent jet (Γ_q and η_q ; e.g., Tchekhovskoy et al. 2008), and the resulting synchrotron maser's peak frequency ν_{pk} (Equation (31)) as a function of angle θ from the jet axis, are represented by the schematic at the top-left corner. The larger interaction region of the flare with the sheath of the jet implies that the observed phase window of the low-frequency bursts is wider than that of the higher-frequency bursts. The shock deceleration radius r_{dec} (Equation (12)) is shorter for flares interacting with the spine of the jet compared to the interaction produced near the sheath. This implies that the high-frequency bursts lead the lower-frequency ones, and are shorter in burst width than the lower-frequency ones ($t_{\text{FRB}} \sim r_{\text{FRB}} / (2\Gamma^2 c)$; Metzger et al. 2019). This frequency-dependent phase window, and the arrival times of bursts, are shown by dividing the jet into three regions, and the corresponding detection phase windows (arbitrary normalization) are represented in the schematic at the top-right corner.

jet (e.g., Γ_q , η_q) are also expected to be structured about the jet axis (Tchekhovskoy et al. 2008). This can influence the region of interaction of the flare ejecta with the structured quiescent jet, and therefore modulate the emission frequency, burst arrival times, and their activity window. This possibility and how it relates to the angular structure of the jet discussed above is illustrated schematically in Figure 5.

Alternatively, some low-frequency FRBs could be bursts of intrinsically higher-frequency viewed slightly off-axis from the

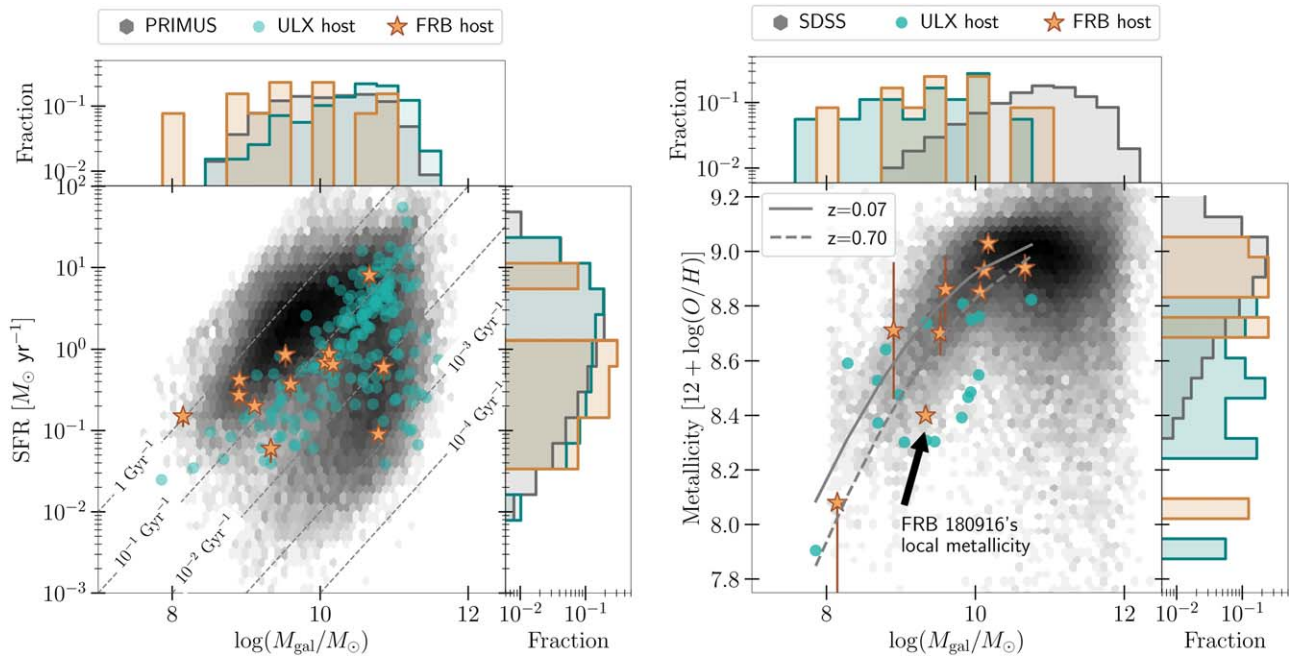


Figure 6. Left panel: the stellar mass and the star formation rate (SFR) of the host galaxies of ULXs (green circles; Kovlakas et al. 2020) and FRBs (brown stars; Heintz et al. 2020), in comparison to a sample of field galaxies from the PRIMUS catalog (gray; Coil et al. 2011). The gray dashed lines denote the contours of specific SFR. The top and right panels denote the distribution of stellar mass and SFR, respectively; dark gray, brown, and green histograms represent the PRIMUS sample, the FRB hosts, and the ULX hosts, respectively. Right panel: the stellar mass and the metallicity of the host galaxies of ULXs and FRBs in comparison to a sample of Sloan Digital Sky Survey (SDSS) emission line star-forming galaxies (gray; e.g., Figure 9 of Heintz et al. 2020). The solid and dashed gray curves denote the empirical mass–metallicity relations (Maiolino et al. 2008) for redshifts $z = 0.07$ and $z = 0.7$, respectively. The local ($\lesssim 60$ pc) metallicity of FRB 180916 (Tendulkar et al. 2021) is also marked for comparison. The top and right panels denote the distribution of stellar mass and metallicity, respectively; dark gray, green, and brown colors represent the SDSS sample, ULX hosts and FRB hosts, respectively.

direction of the emitting shock front (such that the observed emission is Doppler-shifted to lower frequency). In this situation, the peak frequency in the observer frame will decrease, and the burst duration increase, both by the same factor (Beniamini & Kumar 2020), i.e., $\nu_{\text{off}}/\nu_{\text{on}} = t_{\text{off}}/t_{\text{on}}$ (where the subscript off/on corresponds to observed quantities for an observer who is off/on-axis to the direction along the outflow’s velocity). If the relativistic outflow is directed across a narrow range of angles along the core of the jet, this could result in a wider phase window for the low-frequency off-axis bursts.

4. Environmental Implications

4.1. Host Galaxies

Based on Hubble Space Telescope imaging of eight FRB host galaxies with subarcsecond localization, Mannings et al. (2020) found that FRBs reside in IR-fainter regions, consistent with the locations of core collapse SNe but not of the most massive stars (see also Bhandari et al. 2020; Heintz et al. 2020; Li & Zhang 2020). Tendulkar et al. (2021) likewise ruled out significant star formation or an H II region at the location of FRB 180916; their upper limits on the $H\alpha$ luminosity at the burst location constrain potential stellar companions to be cooler than the spectral type O6V. Given the spatial offset of FRB 180916 from the nearest young stellar clump, Tendulkar et al. (2021) further argued for a source age $\gtrsim 0.8$ –7 Myr given the expected range of projected velocities of pulsars, magnetars, or NSs in binaries. These observations are consistent with the scenario described thus far in which FRBs arise from binaries undergoing mass transfer from a companion

star following its main-sequence lifetime, which is $\sim 20(10)$ Myr for a $10(20)M_{\odot}$ star (e.g., Zapartas et al. 2017).

Poutanen et al. (2013) find a spatial correlation in the Antennae galaxies between the ULX sources and young stellar clusters (< 6 Myr). Furthermore, they show that most ULXs are displaced outside of the clusters, suggesting that the massive ULX binaries were ejected out of the star clusters—likely due to strong gravitational encounters. FRBs also show evidence for offsets from regions of intense star formation (Mannings et al. 2020; Tendulkar et al. 2021) and have in at least one case been localized to a region between two potentially interacting galaxies (Law et al. 2020), perhaps akin to a more distant version of the Antennae.

If FRBs arise from mass-transferring binaries similar to ULX sources, they would be expected to occupy similar host galaxies and locations within their hosts. The left panel of Figure 6 shows the star formation rate (SFR) and stellar mass (M_{gal}) of FRB hosts (Heintz et al. 2020) compared to those of ULX hosts (Kovlakas et al. 2020). The hosts of FRBs and ULXs generally form stars at lower rates than in normal galaxies at a given stellar mass (e.g., below the main sequence of the star formation galaxies, or the locus with a higher specific SFR of $\sim 1 \text{ Gyr}^{-1}$; see also Heintz et al. 2020). While the hosts of some FRBs and ULXs are also in the quiescent cloud (e.g., Swartz et al. 2011; Walton et al. 2011; Ravi 2019), they both occur at a greater frequency in hosts with $\text{SFR} \gtrsim 0.1 M_{\odot} \text{ yr}^{-1}$, as seen from the field galaxy population. James et al. (2021) found that the FRB rate, $\Phi(z) \propto (\text{SFR}(z)/\text{SFR}(z=0))^n$, evolves with SFR relative to the cosmological average $\text{SFR}(z)$ with a power-law index $n = 1.36^{+0.25}_{-0.51}$. This is consistent with the SFR-evolution of the ULX population, for which $n = 0.91^{+0.10}_{-0.15}$ (Mapelli et al. 2010).

The FRB hosts are seen to be systematically less massive than those in our ULX sample. As emphasized by Bochenek et al. (2021), comparing FRB host galaxies (typical redshift $z \sim 0.1$ –1) to nearby galaxy populations such as our ULX sample ($\lesssim 40$ Mpc) can be problematic due to the cosmological evolution effects, particularly the shift in star formation to lower-mass galaxies with decreasing redshift. If FRBs indeed trace star formation, this would further exacerbate the tension between ULX and FRB host galaxy masses. On the other hand, the ULX surveys are systematically biased against low-mass galaxies due to selection effects.²⁰

The right panel of Figure 6 compares the metallicities of the FRB and ULX hosts in our sample.²¹ ULXs exhibit a clear preference for lower metallicities (e.g., Mapelli et al. 2010; Walton et al. 2011; Prestwich et al. 2013), which theoretically has been attributed to the prevalence of more massive BHs at low metallicity (e.g., Heger et al. 2003) and other binary evolutionary effects (e.g., Linden et al. 2010; Pavlovskii et al. 2017; Marchant et al. 2017). On the other hand, Figure 6 shows that the FRB host population can also extend to lower metallicities than most of the ULX hosts. At the location of FRB 180916, Tendulkar et al. (2021) found a low metallicity of $12 + \log(\text{O}/\text{H}) \simeq 8.4$ corresponding to $Z \approx Z_{\odot}/2$. Furthermore, the observed ULX population could be biased toward long-lived binary systems, while FRB sources may conversely be produced by binary systems undergoing unstable mass transfer (i.e., those that reach the highest accretion rates; Section 3.2). Systems undergoing unstable mass transfer may preferentially occur at higher metallicity, e.g., due to the dependence of the stability criterion on the mass of the primary BH. A fraction of ULXs may also arise from intermediate-mass BHs (Miller & Colbert 2004), which are potentially too massive to generate the shortest FRBs (Figure 2).

The projected physical offsets of FRB and ULX sources from their respective host galaxy centers are represented in Figure 7. The peaks of the two offset distributions are seen to largely overlap with each other. We note here that our ULX sample is biased against larger offsets²², and the FRBs can exhibit a deficit of short offset sources. The latter may not be an intrinsic effect. The population of FRB sources with small offsets may be underestimated, with decreasing FRB detections from regions closer to the host center. This could be attributed to the increased smearing of the signal by the denser interstellar medium, accompanied by an increase in the DM (e.g., Heintz et al. 2020).

4.2. Local Environment and Nebular Emission

A hallmark of super-Eddington accretion flows is mass-loaded outflows (e.g., Blandford & Begelman 1999; King et al. 2001). ULX systems exhibit direct evidence for winds with

²⁰ An exact comparison between the HECATE-ULX galaxies and the PRIMUS galaxy sample is also complicated by the different indicators (spectral bands) used to determine their respective SFRs. For example, infrared-based SFR indicators are most reliable for late-type galaxies.

²¹ We do not include the ULX samples that host AGNs in our mass-metallicity map. This is because, the oxygen-to-nitrogen-emission line flux ratios are overestimated in AGNs, resulting in an underestimate of the galaxy's metallicity (Nagao et al. 2006; Stampoulis et al. 2019)

²² The ULX sources from the HECATE-ULX sample (Kovlakas et al. 2020) are drawn only from within the D25 region of the host galaxy (i.e., the radius of the isophote where the observed band's surface brightness is 25 mag arcsec⁻²). Therefore, the spatial distribution of the ULXs within their hosts is limited by the radius of the selection region, and is devoid of sources with larger offsets belonging to an exponentially decreasing tail of the distribution.

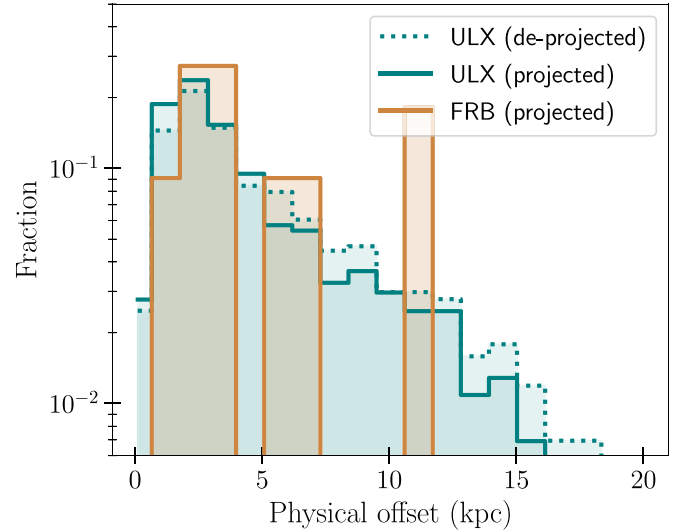


Figure 7. The distributions of the projected physical offsets of ULX (solid green) and FRB (brown) sources from their respective host galactic centers are represented by the solid green and brown histograms, respectively. The dotted green histogram corresponds to the de-projected offsets of ULXs, for comparison. FRB offsets are obtained from Heintz et al. (2020), and the references therein, and ULX offsets are calculated from the HECATE-ULX catalog (Kovlakas et al. 2020).

super-Eddington mechanical powers (Soria et al. 2014) carrying a total energy $\sim 10^{52}$ erg (Roberts et al. 2003), which can exceed the radiative output by up to a factor of 1000 (Pakull et al. 2010).

The mass-loss rate in super-Eddington winds \dot{M}_w is comparable to the binary mass-transfer rate \dot{M}_t (Equation (15)). The density profile of such an outflow of velocity $v_w \sim 0.1c$ (Pinto et al. 2016), at radii much larger than the binary separation, can be approximated as

$$n_w \simeq \frac{\dot{M}_w}{4\pi v_w m_p r^2}. \quad (32)$$

If the accretion disk undergoes precession with a period P (Figure 1), then any ballistic ejection of material along the instantaneous jet direction will encounter the disk wind material from an earlier orientation of the disks by a radial scale no larger than:

$$r_w \sim P \zeta v_w \approx 7.5 \times 10^{15} \text{ cm} \left(\frac{\zeta}{0.3} \right) \left(\frac{P}{100 \text{ d}} \right) \left(\frac{v_w}{0.1c} \right). \quad (33)$$

The Thomson column of this material encountered by an FRB emitted at smaller radii can be estimated as

$$\tau_{T,w} \simeq n_w(r_w) \sigma_T r_w \approx \frac{\dot{M}_w \sigma_T}{4\pi m_p v_w r_w} \sim 1.8 \times 10^{-9} \left(\frac{\dot{M}_w}{\dot{M}_{\text{Edd}}} \right) \left(\frac{m_\bullet}{10} \right) \left(\frac{r_w}{10^{16} \text{ cm}} \right)^{-1} \left(\frac{v_w}{0.1c} \right)^{-1}. \quad (34)$$

For $\dot{M}_w \gg \dot{M}_{\text{Edd}}$, time variability of this column could generate variations in $\text{DM} \approx 5 \times 10^5 \tau_T \text{ pc cm}^{-3}$ over the timescale P , distinct from that accumulated through the quiescent jet cavity (Equation (10)). If the accretion disk wind is magnetized, then propagation through it could generate a more significant local time-variable RM across the active phase (see inset of Figure 1), as observed in FRB 180916 (Pleunis et al. 2021)

and FRB 121102 (Hessels et al. 2019; although the latter could originate from an AGN or a wind-fed nebula on larger scales; Margalit & Metzger 2018). As with the DM above, we estimate the RM contribution through the precessing disk wind (at radii $\gtrsim r_w$) to be

$$\text{RM} \sim \frac{e^3}{2\pi m_e^2 c^4} B_w n_w(r_w) r_w \sin \alpha \approx 0.5 \text{ rad m}^{-2} \left(\frac{\sin \alpha}{0.1} \right) \times \left(\frac{\sigma_w}{0.01} \right)^{1/2} \left(\frac{\dot{M}_w}{\dot{M}_{\text{Edd}}} \right)^{3/2} \left(\frac{m_\bullet}{10} \right)^{3/2} \left(\frac{v_w}{0.1 c} \right)^{-3/2} \left(\frac{r_w}{10^{16} \text{ cm}} \right)^{-2}, \quad (35)$$

where $\sigma_w = B_w^2 / (4\pi n_w m_p c^2)$ is the radially constant magnetization of the wind, and α is an appropriate average angle between the directions of the magnetic field and the FRB path of propagation.

At larger radii $r \sim 10^{17}$ cm, the wind density for fiducial parameters ($\dot{M}_w \sim 10^3 \dot{M}_{\text{Edd}}$; $M_\bullet \sim 10 M_\odot$; $v_w \lesssim 0.1 c$) is $n_w \gtrsim 10 \text{ cm}^{-3}$. This provides the required plasma for self-modulation of the FRB signal (Sobacchi et al. 2021), which predicts the duration of the sub-burst structures to be $\sim 30 \mu\text{s} / \sqrt{n_{w,1}}$.

On yet larger scales of up to hundreds of parsecs, ULX outflows are observed to inflate bubbles of shock-ionized plasma capable of generating persistent optical, X-ray, and radio emission (Pakull & Mirioni 2002; Wang 2002; Kaaret et al. 2003; Ramsey et al. 2006; Soria et al. 2010). The ULX jet also powers steady nonthermal synchrotron emission on smaller scales (Miller et al. 2005; Lang et al. 2007).

Figure 8 compiles detections and upper limits on the persistent radio (top panel) and optical (bottom panel) luminosities of FRBs and ULXs. Although many ULXs are detected, most of the upper limits on FRB persistent source emission are un-constraining due to their comparatively greater distances. Nevertheless, if some FRBs indeed arise from long-lived ULX sources, the closest events may eventually exhibit detectable, and potentially resolvable, persistent emission. This would not necessarily be true for the subset of FRBs arising from short-lived binaries undergoing unstable mass transfer (Section 3), if the system is not active long enough to inflate a large bubble.

The compact synchrotron radio source colocated to < 0.7 pc of FRB 121102 (Chatterjee et al. 2017; Marcote et al. 2017) could arise from a young (\sim decades old) ULX-bubble from a binary system in the process of undergoing unstable mass transfer. The total energy $\sim 10^{50} - 10^{51}$ erg and mass-outflow rate $\dot{M} \sim 10^{19} - 10^{21} \text{ g s}^{-1}$ needed to simultaneously explain the radio spectrum and RM of the source (Margalit & Metzger 2018), are consistent with those expected from super-Eddington disk outflows.

Furthermore, persistent X-ray emission is also expected from FRBs that are produced via the ULX channel. However, due to the large distances of the hitherto detected cosmological FRBs, persistent X-ray emission at the luminosities of ULX sources cannot be detected. The currently tightest constraint indeed comes from one of the nearest repeaters FRB 180916 (at ~ 150 Mpc), for which the 0.5–10 keV is constrained to be $L_X \lesssim 2 \times 10^{40} \text{ erg s}^{-1}$ (Scholz et al. 2020), corresponding to $\sim 10 - 100 L_{\text{Edd}}$ for a BH or NS accretor, respectively. On the other hand, the relatively fainter bursts ($\sim 10^{37} \text{ erg s}^{-1}$; see Figure 2) from the nearest observed repeating FRB 200120 (at

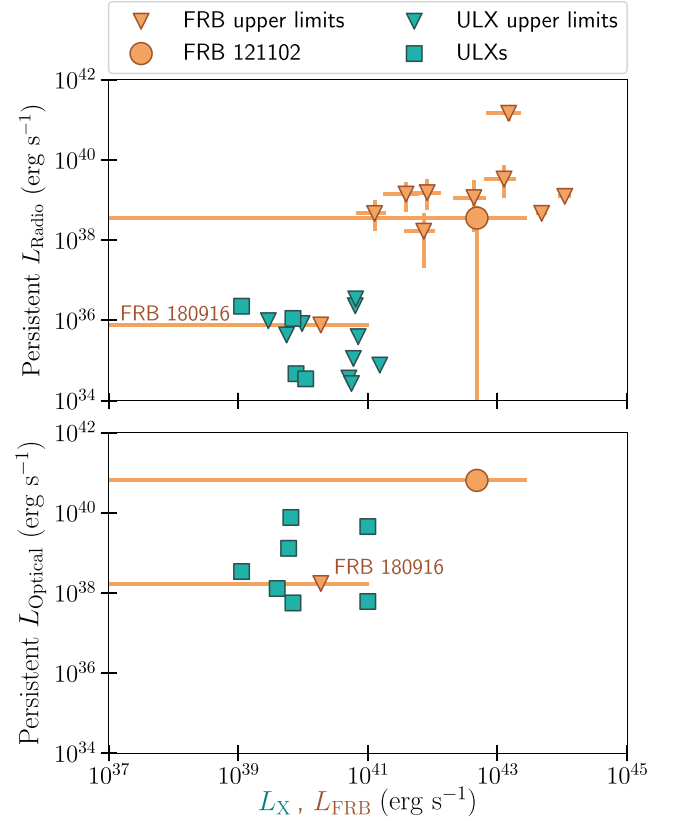


Figure 8. Luminosities of the persistent radio (upper panel) and optical (lower panel) counterparts to FRBs (brown) and ULXs (green) against their respective radio burst or X-ray luminosities (horizontal axis). Detections and upper limits are shown with squares and upside-down triangles, respectively. Persistent radio counterparts and the X-ray luminosities of the represented ULXs are obtained from Kaaret et al. (2003), Miller et al. (2005), Roberts et al. (2006), Mezcuca et al. (2013a, 2013b), Sutton et al. (2013a, 2013b), Luangtip et al. (2016), and Earnshaw et al. (2019). The persistent FRB radio luminosities are obtained from Yang et al. (2020; and the references therein), and the ULX persistent optical counterparts are calculated from the reported optical magnitudes for Holmberg IX X-1, NGC 5204 X-1 (Pakull & Mirioni 2002), Holmberg II X-1 (Lehmann et al. 2005), HLX-1 (Soria et al. 2010), NGC 6946 (Kaaret et al. 2010), NGC 4559 X-10, and NGC 4395 ULX-1 (Vinokurov et al. 2018). The isotropic-equivalent luminosity of the persistent optical counterparts to FRB 121102 and 180916 are calculated from the optical magnitudes reported in Chatterjee et al. (2017) and Tendulkar et al. (2021), respectively.

~ 3.6 Mpc) can be predicted to exhibit an X-ray flux of $\sim 10^{-13} \text{ erg s}^{-1} \text{ cm}^{-2}$ through the accretion channel. This is well below the sensitivity limit of existing X-ray telescopes, consistent with the reported X-ray upper limits from the source error region (Bhardwaj et al. 2021).

4.3. Multiwavelength Transient Counterparts

Models in which FRBs are generated by magnetized shocks predict simultaneous electromagnetic emission ranging from the optical to gamma-ray bands arising from (incoherent) thermal synchrotron emission (e.g., Metzger et al. 2019; Beloborodov 2020). Though carrying more radiated energy than the FRB itself, this counterpart is challenging to detect except for the brightest FRB sources, such as those originating from Galactic magnetar flares. X-rays were observed simultaneously with the FRB-like burst from SGR 1935 + 2154 (e.g.,

Mereghetti et al. 2020), consistent with the predictions of shock synchrotron emission (Metzger et al. 2019; Margalit et al. 2020).

ULXs are known to exhibit fluctuating nonthermal mid-IR outbursts on timescales of a few days that are attributed to their variable jets (e.g., Holmberg IX X-1; Lau et al. 2019). These events can be related to traversing magnetized shocks in precessing jets—that are expected to give rise to an active window of FRBs. Therefore, we strongly encourage simultaneous X-ray and IR monitoring of nearby FRB sources (a few megaparsecs)—especially during the FRB active window, in order to discern their connection to jetted accreting sources.

As discussed in Sections 3.1 and 3.2, the most luminous accretion-powered FRB sources would arise from binary systems undergoing unstable mass transfer. These systems are predicted to be short-lived, with a lifetime of peak FRB activity of $\tau_{\text{unst}} \lesssim$ years to decades (Equation (22)). The end state of this process is a stellar merger or common envelope event (Ivanova et al. 2013).

Stellar merger events are commonly observed in the Milky Way and nearby galaxies as optical (Soker & Tylenda 2006) and/or dusty infrared (Kasliwal et al. 2017) transients. Most such systems are believed to arise from the merger of binaries consisting of main-sequence or moderately evolved stars (e.g., Tylenda et al. 2011), i.e., not containing BH or NS primaries. However, if similar transients are generated from BH/NS merger events (as suggested by numerical simulations; e.g., Law-Smith et al. 2020), then some FRB sources—particularly the most luminous ones—could be accompanied by an LRN in the months to years after “turning off” as FRB sources. More speculatively, the very high BH accretion rates in such events—which are broadly similar to those achieved in tidal disruption events by stellar-mass BHs—could power luminous optical/X-ray transients (e.g., Perets et al. 2016; Kremer et al. 2021), perhaps similar to the “fast blue optical transients” (FBOTs; e.g., Drout et al. 2014; Margutti et al. 2019). FRBs could then serve as unique sign posts to this special type of stellar merger event.

LRNs reach peak optical luminosities in the range $\sim 10^{39}$ – 10^{41} erg s $^{-1}$ (e.g., Pastorello et al. 2019), corresponding to visual apparent magnitudes $\gtrsim 21$ – 22 , at the distance of even the nearest FRB 180916 (≈ 150 Mpc). Such transient emission would be challenging to detect with current optical time-domain facilities, but would make promising targets for future surveys including those conducted with the Vera Rubin Observatory (e.g., LSST Science Collaboration et al. 2009). On the other hand, FBOTs can reach optical peak luminosities and X-ray luminosities up to $\sim 10^{44}$ erg s $^{-1}$, though they can maintain this luminosity only for a few days (e.g., ?). We accordingly recommend that a deep optical/IR and X-ray follow-up campaign be targeted on previously periodic FRB sources that suddenly “turn off” with a \lesssim weekly cadence to capture the brightest phases of putative LRN/FBOT emission.

If the BH spiraling inwards during the common envelope phase generates a relativistic jet, these events could also be a source of high-energy neutrino emission (Grichener & Soker 2021). The end state of such mergers is uncertain, with possibilities ranging from an isolated compact binary with a white dwarf secondary to a quasi-spherical Thorne–Zytkow object (Thorne & Zytkow 1975).

5. Predictions and Conclusions

We have outlined a scenario in which recurring FRBs are powered by transient flares from accreting stellar-mass BH or NS binary systems. The required high accretion rates, which must exceed the Eddington rate to explain the most luminous FRBs, drive us to consider a potential connection to ULX sources, the closest known class of persistent super-Eddington sources. We have provided semiquantitative arguments showing how such systems could in principle account for the observed durations, energetics, beaming fraction, radio frequencies, periodic behavior, rates, and host galaxy properties (with some important caveats). Each of these issues merits more detailed follow-up studies.

We conclude by enumerating a few implications and predictions of the ULX binary scenario.

1. Systems with higher accretion rates generate FRBs with narrower beaming fractions if the latter are shaped by the geometry of the super-Eddington accretion flow (e.g., $f_b \propto \dot{M}_*^{-2}$; Equation (4)). For periodic sources, this could manifest as a narrower active phase with increasing isotropic-equivalent FRB luminosity, i.e., the observed average engine power output (product of burst rate and isotropic-equivalent burst energy) is independent of f_b , for a beam (with a constant opening angle) distributed uniformly in time about the accretion funnel. On the other hand, coupled with the potentially shorter lifetimes of high- \dot{M}_* systems, this results in a lower probability of identifying the most luminous FRB sources as recurring in the first place.
2. The properties of FRB host galaxies, and the spatial offsets of the bursting sources within these galaxies, could track those of the most luminous ULX sources (Figure 6). However, this correspondence may not be perfect, for instance if FRBs preferentially arise from short-lived binaries undergoing unstable mass transfer (and hence are biased against being discovered as persistent ULXs). On smaller spatial scales, some FRB sources will coincide with luminous optical line, X-ray, radio emitting regions akin to the super-bubbles observed surrounding luminous ULXs (Figure 8).
3. A fraction of known ULXs may emit detectable FRBs, and we encourage systematic radio monitoring of these sources. We caution that a rate comparison suggests that atypical conditions—such as a highly magnetized secondary star—may be necessary for ULXs to generate the bulk of the luminous FRBs detected at cosmological distances (Section 3.2). Nevertheless, weaker radio bursts could be detected from a targeted ULX search due to their comparatively closer distances. Evidence for transient ultra-relativistic $\Gamma > 100$ outflows from these systems would also support an FRB connection (Figure 3).
4. Periodic sources could exhibit small systematic variations in the burst DM and RM across the active phase window due to the bursts propagating through the magnetized super-Eddington disk outflows (swept into a spiral pattern intersecting the instantaneous jet axis due to precession of the disk angular momentum). If the quiescent jet is sufficiently dilute, or the disk precession period sufficiently short, the FRB-generating flare will interact with the disk wind, potentially giving rise to a more complicated evolution of the polarization across the burst

than in cases in which the upstream medium is a comparatively organized quiescent jet.

5. The most luminous FRB sources could arise from binaries undergoing unstable mass transfer and evolving toward a merger or common envelope event. To the extent that such sources are periodic, this would lead to systematic variations in the average burst properties with time as the accretion rate rises and the environment surrounding the FRB source evolves toward the final dynamical plunge. Such short-lived sources would not exhibit the large several-parsec-scale nebulae but they could generate compact radio nebulae, perhaps similar to that observed around FRB 121102.

The unstable accreting sources will “turn off” as FRB emitters on a timescale of weeks to years approaching the dynamical phase of the merger. Soon after this point, the system will generate a luminous optical/IR transient, akin to an LRN or dusty infrared transient. More speculatively, the very high BH accretion powers in these systems could power much more luminous optical/X-ray emission, perhaps similar to the observed FBOT transients.

6. Observed FRB durations are consistent with arising from stellar-mass compact objects. However, a similar physical model could in principle be extended to more massive, intermediate-mass or even super-massive BHs. Scaling to the larger ISCO radius (minimum variability time), one would predict the existence of “slow radio bursts” (SRBs) with larger maximum energy and durations significantly longer than hundreds of milliseconds (see Zhang 2020b for a different physical mechanism for generating SRBs). This possibility will be the focus of future work.

Following the submission of this work, a paper by Deng et al. (2021) appeared on a related FRB model invoking transient relativistic ejections from accreting compact objects. Although the details of our models differ, their conclusions broadly mirror those presented here.





This work benefited from the valuable comments from and discussions with Shreya Anand, Wen-fai Fong, Kasper Heintz, Jason Hessels, Phil Kaaret, Jonathan Katz, James Miller-Jones, Douglas Swartz, Shriharsh Tendulkar, and Georgios Vasilopoulos.

N.S. and L.S. are supported by NASA Astrophysics Theory Program (ATP) 80NSSC18K1104 and NSF AST-1716567. B.D.M. acknowledges support from the NASA ATP (grant No. NNX17AK43G), Fermi Guest Investigator Program (grant No. GG016287), and the NSF through the AAG Program (grant No. GG016244). The research of P.B. was funded by the Gordon and Betty Moore Foundation through grant GBMF5076. K.K. acknowledges support from the Swiss National Science Foundation Professorship grant (project No. PP00P2 176868). K.K. received funding from the European Research Council under the European Union’s Seventh Framework Programme (FP/2007-2013) / ERC Grant Agreement No. 617001.

Software: Astropy (Astropy Collaboration et al. 2013, 2018), SciPy (Virtanen et al. 2020).

ORCID iDs

Navin Sridhar  <https://orcid.org/0000-0002-5519-9550>
 Brian D. Metzger  <https://orcid.org/0000-0002-4670-7509>
 Paz Beniamini  <https://orcid.org/0000-0001-7833-1043>

Ben Margalit  <https://orcid.org/0000-0001-8405-2649>
 Mathieu Renzo  <https://orcid.org/0000-0002-6718-9472>
 Lorenzo Sironi  <https://orcid.org/0000-0002-1227-2754>
 Konstantinos Kovlakas  <https://orcid.org/0000-0003-3684-964X>

References

- Abell, G. O., & Margon, B. 1979, *Natur*, **279**, 701
- Abramowicz, M. A., Czerny, B., Lasota, J. P., & Szuszkiewicz, E. 1988, *ApJ*, **332**, 646
- Astropy Collaboration, Price-Whelan, A. M., SipHocz, B. M., et al. 2018, *AJ*, **156**, 123
- Astropy Collaboration, Robitaille, T. P., Tollerud, E. J., et al. 2013, *A&A*, **558**, A33
- Atapin, K. E., & Fabrika, S. N. 2016, *AstL*, **42**, 517
- Babul, A.-N., & Sironi, L. 2020, *MNRAS*, **499**, 2884
- Bachetti, M., Harrison, F. A., Walton, D. J., et al. 2014, *Natur*, **514**, 202
- Begelman, M. C. 2014, arXiv:1410.8132
- Begelman, M. C., King, A. R., & Pringle, J. E. 2006, *MNRAS*, **370**, 399
- Beloborodov, A. M. 2017, *ApJL*, **843**, L26
- Beloborodov, A. M. 2020, *ApJ*, **896**, 142
- Beniamini, P., & Kumar, P. 2020, *MNRAS*, **498**, 651
- Beniamini, P., Wadiasingh, Z., & Metzger, B. D. 2020, *MNRAS*, **496**, 3390
- Bhandari, S., Sadler, E. M., Prochaska, J. X., et al. 2020, *ApJL*, **895**, L37
- Bhardwaj, M., Gaensler, B. M., Kaspi, V. M., et al. 2021, *ApJL*, **910**, L18
- Blagorodnova, N., Klencki, J., Pejcha, O., et al. 2021, arXiv:2102.05662
- Blandford, R. D., & Begelman, M. C. 1999, *MNRAS*, **303**, L1
- Blandford, R. D., & Znajek, R. L. 1977, *MNRAS*, **179**, 433
- Bochenek, C. D., Ravi, V., Belov, K. V., et al. 2020, *Natur*, **587**, 59
- Bochenek, C. D., Ravi, V., & Dong, D. 2021, *ApJL*, **907**, L31
- Brightman, M., Harrison, F. A., Bachetti, M., et al. 2019, *ApJ*, **873**, 115
- Brightman, M., Earnshaw, H., Fürst, F., et al. 2020, *ApJ*, **895**, 127
- Bromberg, O., & Tchekhovskoy, A. 2016, *MNRAS*, **456**, 1739
- Chatterjee, S., Law, C. J., Wharton, R. S., et al. 2017, *Natur*, **541**, 58
- Chen, A. Y., Yuan, Y., Beloborodov, A. M., & Li, X. 2020, arXiv:2010.15619
- CHIME/FRB Collaboration, Andersen, B. C., Bandura, K., et al. 2019, *ApJL*, **885**, L24
- Chime/Frb Collaboration, Amiri, M., Andersen, B. C., et al. 2020, *Natur*, **582**, 351
- Coil, A. L., Blanton, M. R., Burles, S. M., et al. 2011, *ApJ*, **741**, 8
- Connors, R., García, J., Tomsick, J., et al. 2021, *ApJ*, **909**, 146
- Connors, R. M. T., García, J. A., Dauser, T., et al. 2020, *ApJ*, **892**, 47
- Cruces, M., Spitler, L. G., Scholz, P., et al. 2021, *MNRAS*, **500**, 448
- Day, C. K., Deller, A. T., Shannon, R. M., et al. 2020, *MNRAS*, **497**, 3335
- Deng, C.-M., Zhong, S.-Q., & Dai, Z.-G. 2021, arXiv:2102.06796
- Drenkhahn, G., & Spruit, H. C. 2002, *A&A*, **391**, 1141
- Drout, M. R., Chornock, R., Soderberg, A. M., et al. 2014, *ApJ*, **794**, 23
- Earnshaw, H. P., Grefenstette, B. W., Brightman, M., et al. 2019, *ApJ*, **881**, 38
- Fabrika, S. 2004, *ASPRv*, **12**, 1
- Farrell, S. A., Webb, N. A., Barret, D., Godet, O., & Rodrigues, J. M. 2009, *Natur*, **460**, 73
- Fender, R., Wu, K., Johnston, H., et al. 2004, *Natur*, **427**, 222
- Fragile, P. C., Blaes, O. M., Anninos, P., & Salmonson, J. D. 2007, *ApJ*, **668**, 417
- Fragner, M. M., & Nelson, R. P. 2010, *A&A*, **511**, A77
- Frank, J., King, A., & Raine, D. J. 2002, *Accretion Power in Astrophysics* (3rd edn.; Cambridge: Cambridge Univ. Press)
- Gallant, Y. A., Hoshino, M., Langdon, A. B., Arons, J., & Max, C. E. 1992, *ApJ*, **391**, 73
- Gao, Y., Wang, Q. D., Appleton, P. N., & Lucas, R. A. 2003, *ApJL*, **596**, L171
- Globus, N., & Levinson, A. 2013, *PhRvD*, **88**, 084046
- Gourdji, K., Michilli, D., Spitler, L. G., et al. 2019, *ApJL*, **877**, L19
- Granot, J., Komissarov, S. S., & Spitkovsky, A. 2011, *MNRAS*, **411**, 1323
- Grichener, A., & Soker, N. 2021, arXiv:2101.05118
- Grisé, F., Kaaret, P., Corbel, S., Cseh, D., & Feng, H. 2013, *MNRAS*, **433**, 1023
- Heger, A., Fryer, C. L., Woosley, S. E., Langer, N., & Hartmann, D. H. 2003, *ApJ*, **591**, 288
- Heintz, K. E., Prochaska, J. X., Simha, S., et al. 2020, *ApJ*, **903**, 152
- Hessels, J. W. T., Spitler, L. G., Seymour, A. D., et al. 2019, *ApJL*, **876**, L23
- Hillwig, T. C., & Gies, D. R. 2008, *ApJL*, **676**, L37
- Ioka, K., & Zhang, B. 2020, *ApJL*, **893**, L26
- Israel, G. L., Belfiore, A., Stella, L., et al. 2017, *Sci*, **355**, 817
- Ivanova, N., Justham, S., Chen, X., et al. 2013, *A&ARv*, **21**, 59

- Iwamoto, M., Amano, T., Hoshino, M., & Matsumoto, Y. 2018, *ApJ*, **858**, 93
- James, C. W., Prochaska, J. X., Macquart, J. P., et al. 2021, arXiv:2101.07998
- Kaaret, P., Corbel, S., Prestwich, A. H., & Zezas, A. 2003, *Sci*, **299**, 365
- Kaaret, P., & Feng, H. 2009, *ApJ*, **702**, 1679
- Kaaret, P., Feng, H., & Roberts, T. P. 2017, *ARA&A*, **55**, 303
- Kaaret, P., Feng, H., Wong, D. S., & Tao, L. 2010, *ApJL*, **714**, L167
- Kasliwal, M. M., et al. 2017, *Sci*, **358**, 1559
- Katz, J. I. 1973, *NPhS*, **246**, 87
- Katz, J. I. 1977, *ApJ*, **215**, 265
- Katz, J. I. 1981, *A&A*, **95**, L15
- Katz, J. I. 2016, *ApJ*, **826**, 226
- Katz, J. I. 2017, *MNRAS*, **471**, L92
- Katz, J. I. 2020, *MNRAS*, **494**, L64
- Katz, J. I. 2021, *MNRAS*, **502**, 4664
- Katz, J. I., Anderson, S. F., Margon, B., & Grandi, S. A. 1982, *ApJ*, **260**, 780
- Keane, E. F., Stappers, B. W., Kramer, M., & Lyne, A. G. 2012, *MNRAS*, **425**, L71
- King, A. R. 2009, *MNRAS*, **393**, L41
- King, A. R., & Begelman, M. C. 1999, *ApJL*, **519**, L169
- King, A. R., Davies, M. B., Ward, M. J., Fabbiano, G., & Elvis, M. 2001, *ApJL*, **552**, L109
- Kochanek, C. S., Adams, S. M., & Belczynski, K. 2014, *MNRAS*, **443**, 1319
- Kolb, U. 1998, *MNRAS*, **297**, 419
- Kovlakas, K., Zezas, A., Andrews, J. J., et al. 2020, *MNRAS*, **498**, 4790
- Kremer, K., Lu, W., Piro, A. L., et al. 2021, *ApJ*, **911**, 104
- Kulkarni, S. R., Ofek, E. O., Neill, J. D., Zheng, Z., & Juric, M. 2014, *ApJ*, **797**, 70
- Kumar, P., & Bošnjak, Ž. 2020, *MNRAS*, **494**, 2385
- Kumar, P., Lu, W., & Bhattacharya, M. 2017, *MNRAS*, **468**, 2726
- Kumar, P., & Zhang, B. 2015, *PhR*, **561**, 1
- Lang, C. C., Kaaret, P., Corbel, S., & Mercer, A. 2007, *ApJ*, **666**, 79
- Lau, R. M., Heida, M., Walton, D. J., et al. 2019, *ApJ*, **878**, 71
- Law, C. J., Butler, B. J., Prochaska, J. X., et al. 2020, *ApJ*, **899**, 161
- Law-Smith, J. A. P., Everson, R. W., Ramirez-Ruiz, E., et al. 2020, arXiv:2011.06630
- Lehmann, I., Becker, T., Fabrika, S., et al. 2005, *A&A*, **431**, 847
- Levin, Y., Beloborodov, A. M., & Bransgrove, A. 2020, *ApJL*, **895**, L30
- Levine, A. M., & Jernigan, J. G. 1982, *ApJ*, **262**, 294
- Li, C. K., Lin, L., Xiong, S. L., et al. 2021, *NatAs*, in press
- Li, D., & Zanazzi, J. J. 2021, *ApJL*, **909**, L25
- Li, Y., & Zhang, B. 2020, *ApJL*, **899**, L6
- Linden, T., Kalogera, V., Sepinsky, J. F., et al. 2010, *ApJ*, **725**, 1984
- Lithwick, Y., & Sari, R. 2001, *ApJ*, **555**, 540
- Lorimer, D. R., Bailes, M., McLaughlin, M. A., Narkevic, D. J., & Crawford, F. 2007, *Sci*, **318**, 777
- LSST Science Collaboration, Abell, P. A., Allison, J., et al. 2009, arXiv:0912.0201
- Lu, W., & Kumar, P. 2016, *MNRAS*, **461**, L122
- Lu, W., & Kumar, P. 2018, *MNRAS*, **477**, 2470
- Lu, W., Piro, A. L., & Waxman, E. 2020, *MNRAS*, **498**, 1973
- Luangtip, W., Roberts, T. P., & Done, C. 2016, *MNRAS*, **460**, 4417
- Luo, R., Wang, B. J., Men, Y. P., et al. 2020, *Natur*, **586**, 693
- Lyubarsky, Y. 2008, *ApJ*, **682**, 1443
- Lyubarsky, Y. 2014, *MNRAS*, **442**, L9
- Lyubarsky, Y. 2019, *MNRAS*, **483**, 1731
- Lyubarsky, Y. 2020, *ApJ*, **897**, 1
- Lyutikov, M., Barkov, M. V., & Giannios, D. 2020, *ApJL*, **893**, L39
- MacLeod, M., & Loeb, A. 2020, *ApJ*, **895**, 29
- Mahmann, J. F., Levinson, A., & Aloy, M. A. 2020, *MNRAS*, **494**, 4203
- Maiolino, R., Nagao, T., Grazian, A., et al. 2008, *A&A*, **488**, 463
- Mannings, A. G., Fong, W.-F., Simha, S., et al. 2020, arXiv:2012.11617
- Mapelli, M., Ripamonti, E., Zampieri, L., Colpi, M., & Bressan, A. 2010, *MNRAS*, **408**, 234
- Marchant, P., Langer, N., Podsiadlowski, P., et al. 2017, *A&A*, **604**, A55
- Marcote, B., Paragi, Z., Hessels, J. W. T., et al. 2017, *ApJL*, **834**, L8
- Margalit, B., Berger, E., & Metzger, B. D. 2019, *ApJ*, **886**, 110
- Margalit, B., & Metzger, B. D. 2018, *ApJL*, **868**, L4
- Margalit, B., Metzger, B. D., & Sironi, L. 2020, *MNRAS*, **494**, 4627
- Margon, B. 1984, *ARA&A*, **22**, 507
- Margutti, R., Metzger, B. D., Chornock, R., et al. 2019, *ApJ*, **872**, 18
- Mereghetti, S., Savchenko, V., Ferrigno, C., et al. 2020, *ApJL*, **898**, L29
- Metzger, B. D., Berger, E., & Margalit, B. 2017, *ApJ*, **841**, 14
- Metzger, B. D., Margalit, B., & Sironi, L. 2019, *MNRAS*, **485**, 4091
- Mezcua, M., Farrell, S. A., Gladstone, J. C., & Lobanov, A. P. 2013a, *MNRAS*, **436**, 1546
- Mezcua, M., Roberts, T. P., Sutton, A. D., & Lobanov, A. P. 2013b, *MNRAS*, **436**, 3128
- Michilli, D., Seymour, A., Hessels, J. W. T., et al. 2018, *Natur*, **553**, 182
- Middleton, M. J., Fragile, P. C., Ingram, A., & Roberts, T. P. 2019, *MNRAS*, **489**, 282
- Miller, M. C., & Colbert, E. J. M. 2004, *IJMPD*, **13**, 1
- Miller, N. A., Mushotzky, R. F., & Neff, S. G. 2005, *ApJL*, **623**, L109
- Miller-Jones, J. C. A., Fender, R. P., & Nakar, E. 2006, *MNRAS*, **367**, 1432
- Mineo, S., Gilfanov, M., & Sunyaev, R. 2012, *MNRAS*, **419**, 2095
- Mioduszewski, A. J., Rupen, M. P., Walker, R. C., Schillemat, K. M., & Taylor, G. B. 2004, AAS/High Energy Astrophysics Division, **8**, 29.03
- Mirabel, I. F., & Rodríguez, L. F. 1994, *Natur*, **371**, 46
- Motch, C., Pakull, M. W., Soria, R., Grisé, F., & Pietrzyński, G. 2014, *Natur*, **514**, 198
- Mushtukov, A. A., Suleimanov, V. F., Tsygankov, S. S., & Poutanen, J. 2015, *MNRAS*, **454**, 2539
- Nagao, T., Maiolino, R., & Marconi, A. 2006, *A&A*, **459**, 85
- Narayan, R., & Yi, I. 1995, *ApJ*, **452**, 710
- Nicholl, M., et al. 2017, *ApJL*, **848**, L18
- Paczynski, B. 1971, *ARA&A*, **9**, 183
- Pakull, M. W., & Mirioni, L. 2002, arXiv:astro-ph/0202488
- Pakull, M. W., Soria, R., & Motch, C. 2010, *Natur*, **466**, 209
- Parfrey, K., Giannios, D., & Beloborodov, A. M. 2015, *MNRAS*, **446**, L61
- Parfrey, K., Spitkovsky, A., & Beloborodov, A. M. 2016, *ApJ*, **822**, 33
- Parfrey, K., & Tchekhovskoy, A. 2017, *ApJL*, **851**, L34
- Pastor-Marazuela, I., Connor, L., van Leeuwen, J., et al. 2020, arXiv:2012.08348
- Pastorello, A., Mason, E., Taubenberger, S., et al. 2019, *A&A*, **630**, A75
- Pavlovskii, K., Ivanova, N., Belczynski, K., & Van, K. X. 2017, *MNRAS*, **465**, 2092
- Pejcha, O. 2014, *ApJ*, **788**, 22
- Pejcha, O., Metzger, B. D., Tyles, J. G., & Tomida, K. 2017, *ApJ*, **850**, 59
- Perets, H. B., Li, Z., Lombardi, J. C., Milcarek, J., & Stephen, R. J. 2016, *ApJ*, **823**, 113
- Petroff, E., Barr, E. D., Jameson, A., et al. 2016, *PASA*, **33**, e045
- Philippov, A., Uzdensky, D. A., Spitkovsky, A., & Cerutti, B. 2019, *ApJL*, **876**, L6
- Phinney, E. S. 1982, *MNRAS*, **198**, 1109
- Pinto, C., Middleton, M. J., & Fabian, A. C. 2016, *Natur*, **533**, 64
- Platts, E., Weltman, A., Walters, A., et al. 2019, *PhR*, **821**, 1
- Pleunis, Z., Michilli, D., Bassa, C. G., et al. 2021, *ApJL*, **911**, L3
- Plotnikov, I., & Sironi, L. 2019, *MNRAS*, **485**, 3816
- Popov, S. B., & Postnov, K. A. 2013, arXiv:1307.4924
- Poutanen, J., Fabrika, S., Valeev, A. F., Sholukhova, O., & Greiner, J. 2013, *MNRAS*, **432**, 506
- Poutanen, J., Lipunova, G., Fabrika, S., Butkevich, A. G., & Abolmasov, P. 2007, *MNRAS*, **377**, 1187
- Prestwich, A. H., Tsantaki, M., Zezas, A., et al. 2013, *ApJ*, **769**, 92
- Rajwade, K. M., Mickaliger, M. B., Stappers, B. W., et al. 2020, *MNRAS*, **495**, 3551
- Ramsey, C. J., Williams, R. M., Gruendl, R. A., et al. 2006, *ApJ*, **641**, 241
- Rappaport, S. A., Podsiadlowski, P., & Pfahl, E. 2005, *MNRAS*, **356**, 401
- Ravi, V. 2019, *NatAs*, **3**, 928
- Ripperda, B., Porth, O., Sironi, L., & Keppens, R. 2019, *MNRAS*, **485**, 299
- Roberts, T. P., Goad, M. R., Ward, M. J., & Warwick, R. S. 2003, *MNRAS*, **342**, 709
- Roberts, T. P., Kilgard, R. E., Warwick, R. S., Goad, M. R., & Ward, M. J. 2006, *MNRAS*, **371**, 1877
- Rodríguez Castillo, G. A., Israel, G. L., Belfiore, A., et al. 2020, *ApJ*, **895**, 60
- Safarzadeh, M., Prochaska, J. X., Heintz, K. E., & Fong, W.-F. 2020, *ApJ*, **905**, L30
- Sarazin, C. L., Begelman, M. C., & Hatchett, S. P. 1980, *ApJL*, **238**, L129
- Sari, R., & Piran, T. 1995, *ApJL*, **455**, L143
- Schneider, F. R. N., Ohlmann, S. T., Podsiadlowski, P., et al. 2019, *Natur*, **574**, 211
- Scholz, P., Cook, A., Cruces, M., et al. 2020, *ApJ*, **901**, 165
- Shakura, N. I., & Sunyaev, R. A. 1973, *A&A*, **500**, 33
- Shultz, M., Wade, G. A., Alecian, E., & BinaMiCS Collaboration 2015, *MNRAS*, **454**, L1
- Sobacchi, E., Lyubarsky, Y., Beloborodov, A. M., & Sironi, L. 2021, *MNRAS*, **500**, 272
- Soker, N., & Tylenda, R. 2006, *MNRAS*, **373**, 733
- Soria, R., Hau, G. K. T., Graham, A. W., et al. 2010, *MNRAS*, **405**, 870
- Soria, R., Long, K. S., Blair, W. P., et al. 2014, *Sci*, **343**, 1330
- Spitler, L. G., Scholz, P., Hessels, J. W. T., et al. 2016, *Natur*, **531**, 202
- Spruit, H. C., & Uzdensky, D. A. 2005, *ApJ*, **629**, 960

- Sridhar, N., Bhattacharyya, S., Chandra, S., & Antia, H. M. 2019, *MNRAS*, **487**, 4221
- Sridhar, N., García, J. A., Steiner, J. F., et al. 2020, *ApJ*, **890**, 53
- Sridhar, N., Zrake, J., Metzger, B. D., Sironi, L., & Giannios, D. 2021, *MNRAS*, **501**, 3184
- Stampoulis, V., van Dyk, D. A., Kashyap, V. L., & Zezas, A. 2019, *MNRAS*, **485**, 1085
- Stone, N., & Loeb, A. 2012, *PhRvL*, **108**, 061302
- Sutton, A. D., Roberts, T. P., Gladstone, J. C., et al. 2013a, *MNRAS*, **434**, 1702
- Sutton, A. D., Roberts, T. P., & Middleton, M. J. 2013b, *MNRAS*, **435**, 1758
- Swartz, D. A., Soria, R., Tennant, A. F., & Yukita, M. 2011, *ApJ*, **741**, 49
- Tanaka, Y., & Shibazaki, N. 1996, *ARA&A*, **34**, 607
- Tchekhovskoy, A., McKinney, J. C., & Narayan, R. 2008, *MNRAS*, **388**, 551
- Tchekhovskoy, A., Narayan, R., & McKinney, J. C. 2010, *ApJ*, **711**, 50
- Tchekhovskoy, A., Narayan, R., & McKinney, J. C. 2011, *MNRAS*, **418**, L79
- Tendulkar, S. P., Bassa, C. G., Cordes, J. M., et al. 2017, *ApJL*, **834**, L7
- Tendulkar, S. P., Gil de Paz, A., Kirichenko, A. Y., et al. 2021, *ApJL*, **908**, L12
- Tetarenko, B. E., Sivakoff, G. R., Heinke, C. O., & Gladstone, J. C. 2016, *ApJS*, **222**, 15
- The CHIME/FRB Collaboration, Andersen, B. C., Bandura, K. M., et al. 2020, *Natur*, **587**, 54
- Thorne, K. S., & Zytlow, A. N. 1975, *ApJL*, **199**, L19
- Thornton, D., Stappers, B., Bailes, M., et al. 2013, *Sci*, **341**, 53
- Tsygankov, S. S., Mushtukov, A. A., Suleimanov, V. F., & Poutanen, J. 2016, *MNRAS*, **457**, 1101
- Tylenda, R., Hajduk, M., Kamiński, T., et al. 2011, *A&A*, **528**, A114
- Vasilopoulos, G., Lander, S. K., Koliopanos, F., & Bailyn, C. D. 2020, *MNRAS*, **491**, 4949
- Vinokurov, A., Fabrika, S., & Atapin, K. 2018, *ApJ*, **854**, 176
- Virtanen, P., Gommers, R., Oliphant, T. E., et al. 2020, *NatMe*, **17**, 261
- Wadiasingh, Z., Beniamini, P., Timokhin, A., et al. 2020, *ApJ*, **891**, 82
- Wadiasingh, Z., & Timokhin, A. 2019, *ApJ*, **879**, 4
- Walton, D. J., Fürst, F., Bachetti, M., et al. 2016, *ApJL*, **827**, L13
- Walton, D. J., Gladstone, J. C., Roberts, T. P., & Fabian, A. C. 2011, *AN*, **332**, 354
- Wang, Q. D. 2002, *MNRAS*, **332**, 764
- Waxman, E. 2017, *ApJ*, **842**, 34
- Weng, S.-S., & Feng, H. 2018, *ApJ*, **853**, 115
- Wiktorowicz, G., Sobolewska, M., Sadowski, A., & Belczynski, K. 2015, *ApJ*, **810**, 20
- Yang, Y.-P., Li, Q.-C., & Zhang, B. 2020, *ApJ*, **895**, 7
- Yuan, F., & Narayan, R. 2014, *ARA&A*, **52**, 529
- Yuan, Y., Beloborodov, A. M., Chen, A. Y., & Levin, Y. 2020, *ApJL*, **900**, L21
- Zanazzi, J. J., & Lai, D. 2020, *ApJL*, **892**, L15
- Zapartas, E., de Mink, S. E., Izzard, R. G., et al. 2017, *A&A*, **601**, A29
- Zhang, B. 2020a, *Natur*, **587**, 45
- Zhang, B. 2020b, *ApJL*, **890**, L24
- Zhong, S.-Q., & Dai, Z.-G. 2020, *ApJ*, **893**, 9
- Zrake, J., & Arons, J. 2017, *ApJ*, **847**, 57